

# Measurement and analysis of the $^{241}\text{Am}$ neutron capture cross section at the n\_TOF facility at CERN

---

(n\_TOF Collaboration) Mendoza, E.; ...; Bosnar, Damir; ...; Žugec, Petar

Source / Izvornik: **Physical Review C, 2018, 97**

**Journal article, Published version**

**Rad u časopisu, Objavljena verzija rada (izdavačev PDF)**

<https://doi.org/10.1103/PhysRevC.97.054616>

Permanent link / Trajna poveznica: <https://urn.nsk.hr/urn:nbn:hr:217:419417>

Rights / Prava: [Attribution 4.0 International](#)/[Imenovanje 4.0 međunarodna](#)

Download date / Datum preuzimanja: **2025-03-29**



Repository / Repozitorij:

[Repository of the Faculty of Science - University of Zagreb](#)



**Measurement and analysis of the  $^{241}\text{Am}$  neutron capture cross section at the n\_TOF facility at CERN**

E. Mendoza,<sup>1,\*</sup> D. Cano-Ott,<sup>1</sup> S. Altstadt,<sup>2</sup> S. Andriamonje,<sup>3</sup> J. Andrzejewski,<sup>4</sup> L. Audouin,<sup>5</sup> J. Balibrea,<sup>1</sup> V. Bécáres,<sup>1</sup> M. Barbagallo,<sup>6</sup> F. Bečvář,<sup>7</sup> F. Belloni,<sup>3</sup> B. Berthier,<sup>5</sup> E. Berthoumieux,<sup>3</sup> J. Billowes,<sup>8</sup> D. Bosnar,<sup>9</sup> M. Brugger,<sup>10</sup> F. Calviño,<sup>11</sup> M. Calviani,<sup>10</sup> C. Carrapiço,<sup>12</sup> F. Cerutti,<sup>10</sup> E. Chiaveri,<sup>10,3</sup> M. Chin,<sup>10</sup> N. Colonna,<sup>6</sup> G. Cortés,<sup>11</sup> M. A. Cortés-Giraldo,<sup>13</sup> M. Diakaki,<sup>14</sup> I. Dillmann,<sup>15</sup> C. Domingo-Pardo,<sup>2</sup> I. Durán,<sup>16</sup> N. Dzysiuk,<sup>17</sup> C. Eleftheriadis,<sup>18</sup> A. Ferrari,<sup>10</sup> K. Fraval,<sup>3</sup> V. Furman,<sup>19</sup> M. B. Gómez-Hornillos,<sup>11</sup> S. Ganesan,<sup>20</sup> A. R. García,<sup>1</sup> G. Giubrone,<sup>21</sup> I. F. Gonçalves,<sup>12</sup> E. González,<sup>1</sup> A. Goverdovski,<sup>22</sup> F. Gramegna,<sup>17</sup> E. Griesmayer,<sup>23</sup> C. Guerrero,<sup>10,13</sup> F. Gunsing,<sup>3</sup> P. Gurusamy,<sup>20</sup> T. Heftrich,<sup>2</sup> S. Heintz,<sup>24</sup> A. Hernández-Prieto,<sup>10,11</sup> J. Heyse,<sup>25</sup> D. G. Jenkins,<sup>26</sup> E. Jericha,<sup>23</sup> F. Käppeler,<sup>27</sup> Y. Kadi,<sup>10</sup> D. Karadimos,<sup>14</sup> T. Katabuchi,<sup>28</sup> V. Ketlerov,<sup>22</sup> V. Khryachkov,<sup>22</sup> P. Koehler,<sup>29</sup> M. Kokkoris,<sup>14</sup> J. Kroll,<sup>7</sup> M. Krtička,<sup>7</sup> C. Lampoudis,<sup>3</sup> C. Langer,<sup>2</sup> E. Leal-Cidoncha,<sup>16</sup> C. Lederer,<sup>30</sup> H. Leeb,<sup>23</sup> L. S. Leong,<sup>5</sup> J. Lerendegui-Marco,<sup>13</sup> M. Licata,<sup>31,32</sup> D. López,<sup>1</sup> R. Losito,<sup>10</sup> A. Manousos,<sup>18</sup> J. Marganiec,<sup>4</sup> T. Martínez,<sup>1</sup> C. Massimi,<sup>31,32</sup> P. Mastinu,<sup>17</sup> M. Mastromarco,<sup>6</sup> A. Mengoni,<sup>33</sup> P. M. Milazzo,<sup>34</sup> F. Mingrone,<sup>31</sup> M. Mirea,<sup>35</sup> W. Mondelaers,<sup>25</sup> C. Paradela,<sup>16</sup> A. Pavlik,<sup>30</sup> J. Perkowski,<sup>4</sup> A. J. M. Plompen,<sup>25</sup> J. Praena,<sup>13,36</sup> J. M. Quesada,<sup>13</sup> T. Rauscher,<sup>37</sup> R. Reifarh,<sup>2</sup> A. Riego-Perez,<sup>11</sup> M. Robles,<sup>16</sup> F. Roman,<sup>35</sup> C. Rubbia,<sup>10</sup> J. A. Ryan,<sup>8</sup> M. Sabaté-Gilarte,<sup>10,13</sup> R. Sarmiento,<sup>12</sup> A. Saxena,<sup>20</sup> P. Schillebeeckx,<sup>25</sup> S. Schmidt,<sup>2</sup> D. Schumann,<sup>24</sup> P. Sedyshev,<sup>19</sup> G. Tagliente,<sup>6</sup> J. L. Tain,<sup>21</sup> A. Tarifeño-Saldivia,<sup>21</sup> D. Tarrío,<sup>16</sup> L. Tassan-Got,<sup>5</sup> A. Tsinganis,<sup>10</sup> S. Valenta,<sup>7</sup> G. Vannini,<sup>31,32</sup> V. Variale,<sup>6</sup> P. Vaz,<sup>12</sup> A. Ventura,<sup>31</sup> M. J. Vermeulen,<sup>26</sup> R. Versaci,<sup>10</sup> V. Vlachoudis,<sup>10</sup> R. Vlastou,<sup>14</sup> A. Wallner,<sup>38</sup> T. Ware,<sup>8</sup> M. Weigand,<sup>2</sup> C. Weiss,<sup>23</sup> T. Wright,<sup>8</sup> and P. Žugec<sup>9</sup>

(n\_TOF Collaboration)

<sup>1</sup>Centro de Investigaciones Energéticas Medioambientales y Tecnológicas (CIEMAT), Spain

<sup>2</sup>Goethe University Frankfurt, Germany

<sup>3</sup>CEA Saclay, Irfu, Gif-sur-Yvette, France

<sup>4</sup>University of Lodz, Poland

<sup>5</sup>Institut de Physique Nucléaire, CNRS-IN2P3, Université Paris-Sud, Université Paris-Saclay,

F-91406 Orsay Cedex, France

<sup>6</sup>Istituto Nazionale di Fisica Nucleare, Sezione di Bari, Italy

<sup>7</sup>Charles University, Prague, Czech Republic

<sup>8</sup>University of Manchester, United Kingdom

<sup>9</sup>Department of Physics, Faculty of Science, University of Zagreb, Croatia

<sup>10</sup>European Organization for Nuclear Research (CERN), Switzerland

<sup>11</sup>Universitat Politècnica de Catalunya, Spain

<sup>12</sup>Instituto Superior Técnico, Lisbon, Portugal

<sup>13</sup>Universidad de Sevilla, Spain

<sup>14</sup>National Technical University of Athens, Greece

<sup>15</sup>Technische Universität München, Garching, Germany

<sup>16</sup>University of Santiago de Compostela, Spain

<sup>17</sup>Istituto Nazionale di Fisica Nucleare, Sezione di Legnaro, Italy

<sup>18</sup>Aristotle University of Thessaloniki, Thessaloniki, Greece

<sup>19</sup>Joint Institute for Nuclear Research (JINR), Dubna, Russia

<sup>20</sup>Bhabha Atomic Research Centre (BARC), India

<sup>21</sup>Instituto de Física Corpuscular, Universidad de Valencia, Spain

<sup>22</sup>Institute of Physics and Power Engineering (IPPE), Obninsk, Russia

<sup>23</sup>Technische Universität Wien, Austria

<sup>24</sup>Paul Scherrer Institut (PSI), Villingen, Switzerland

<sup>25</sup>European Commission, Joint Research Centre, Geel, Retieseweg 111, B-2440 Geel, Belgium

<sup>26</sup>University of York, United Kingdom

<sup>27</sup>Karlsruhe Institute of Technology, Campus North, IKP, 76021 Karlsruhe, Germany

<sup>28</sup>Tokyo Institute of Technology, Japan

<sup>29</sup>Oak Ridge National Laboratory (ORNL), Oak Ridge, Tennessee 37831, USA

<sup>30</sup>University of Vienna, Faculty of Physics, Vienna, Austria

<sup>31</sup>Istituto Nazionale di Fisica Nucleare, Sezione di Bologna, Italy

<sup>32</sup>Dipartimento di Fisica e Astronomia, Università di Bologna, Italy

<sup>33</sup>Agenzia nazionale per le nuove tecnologie (ENEA), Bologna, Italy

<sup>34</sup>Istituto Nazionale di Fisica Nucleare, Sezione di Trieste, Italy

<sup>35</sup>Horia Hulubei National Institute of Physics and Nuclear Engineering, Romania

<sup>36</sup>Universidad de Granada, Spain

<sup>37</sup>*Department of Physics, University of Basel, Switzerland*<sup>38</sup>*Australian National University, Canberra, Australia*

(Received 31 January 2018; published 24 May 2018)

The  $^{241}\text{Am}(n,\gamma)$  cross section has been measured at the n\_TOF facility at CERN with the n\_TOF BaF<sub>2</sub> Total Absorption Calorimeter in the energy range between 0.2 eV and 10 keV. Our results are analyzed as resolved resonances up to 700 eV, allowing a more detailed description of the cross section than in the current evaluations, which contain resolved resonances only up to 150–160 eV. The cross section in the unresolved resonance region is perfectly consistent with the predictions based on the average resonance parameters deduced from the resolved resonances, thus obtaining a consistent description of the cross section in the full neutron energy range under study. Below 20 eV, our results are in reasonable agreement with JEFF-3.2 as well as with the most recent direct measurements of the resonance integral, and differ up to 20–30% with other experimental data. Between 20 eV and 1 keV, the disagreement with other experimental data and evaluations gradually decreases, in general, with the neutron energy. Above 1 keV, we find compatible results with previously existing values.

DOI: [10.1103/PhysRevC.97.054616](https://doi.org/10.1103/PhysRevC.97.054616)

## I. INTRODUCTION

To improve the design of new advanced nuclear reactors and for determining their performance in the transmutation of nuclear waste, it is important to reduce the present neutron cross section uncertainties of minor actinides [1–3]. In particular,  $^{241}\text{Am}$  is one of the most abundant minor actinides in spent fuels, and capture is the dominant reaction in this nucleus at low neutron energies. In addition, the reprocessing of Am is technologically more advanced than for other minor actinides.

Improved experimental cross section data for the  $^{241}\text{Am}(n,\gamma)$  reaction was one of the objectives of the ANDES project within the Seventh Framework Programme of the European Commission. Therefore, four time-of-flight (TOF) measurements were planned and carried out. In this paper we present the results of one of these measurements. The other three have been already published: one of them, which is also a capture measurement, was performed with the same sample and in the same facility but with different  $\gamma$ -ray detectors [4]; the other two are a transmission and a capture measurement performed at JRC-Geel, with a different sample [5]. In addition there are several other measurements, both TOF and integral, which present significant discrepancies among one another. As a consequence, it is not surprising that there are also large discrepancies among the evaluated libraries. Indeed, these discrepancies are being investigated through an international collaborative working group organized by NEA-OECD [6].

The  $^{241}\text{Am}(n,\gamma)$  cross section measurement presented in this paper was performed at the n\_TOF facility at CERN [7] using the n\_TOF Total Absorption Calorimeter (TAC). Capture cross section data were obtained for incident neutron energies between 0.2 eV and 10 keV. In Sec. II we describe the experimental setup. The data reduction procedures to derive

the experimental capture yield, which will be made available for the EXFOR database [8], are presented in Sec. III. The results of a resonance shape analysis are reported in Sec. IV and compared with results of other experiments and evaluations in Sec. V. Finally, the conclusions of this work are presented in Sec. VI.

## II. THE EXPERIMENTAL SETUP

### A. The n\_TOF facility at CERN

The n\_TOF facility at CERN [7,9,10] is a high instantaneous intensity pulsed neutron source designed to study neutron-nucleus interactions for neutron kinetic energies ranging from a few meV to several GeV. Neutrons are produced every 1.2 s (or multiples of this interval) from spallation reactions by a 20 GeV/*c* proton beam delivered by the CERN Proton Synchrotron (PS) with 16 ns FWHM time resolution impinging on a 1.3 tonne cylindrical lead target 40 cm in length and 60 cm in diameter. The target is surrounded by a coolant circuit of 1-cm-thick water, followed by 4 cm of borated water (H<sub>2</sub>O + 1.28% H<sub>3</sub>BO<sub>3</sub>, fraction in mass) which moderates the initially fast neutron spectrum.<sup>1</sup> At present neutrons travel through two evacuated beam lines, a horizontal and a vertical one at angles of 10° and 90° with respect to the direction of the proton beam, respectively. However, the vertical beam line [11] had not been built when this measurement was made in 2010. The horizontal beam line reaches a measuring station located at a distance of 182.3 m from the spallation target and has a length of 7.9 m. A sweeping magnet placed along the beam line prevents the charged particles from reaching the measuring station and two collimators give the appropriate shape to the neutron beam.

There are about  $1.2 \times 10^5$  neutrons per nominal pulse of  $7 \times 10^{12}$  protons between 0.1 eV and 10 keV reaching the irradiation position. The energy dependence of the neutron beam was determined with three different detectors [12]: a

\*emilio.mendoza@ciemat.es

<sup>1</sup>The n\_TOF facility was closed at the end of the 2004 campaign. It was opened again in 2009 (Phase-II), with a different lead block and coolant circuit, which are the ones described here.

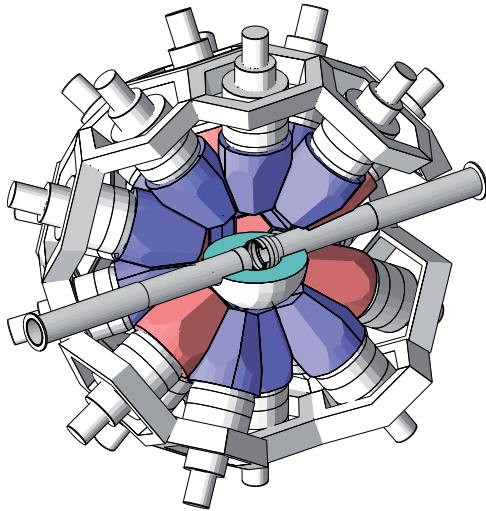


FIG. 1. Schematic view of part of the n\_TOF Total Absorption Calorimeter. Modules in front of the beam pipe and the upper hemisphere of the neutron absorber are not shown.

silicon flux monitor [13] (SiMon), a Micromegas gas detector [14], and a calibrated fission chamber from Physikalisch Technische Bundesanstalt (PTB) [15], which are based on the  $^6\text{Li}(n,t)$ ,  $^{10}\text{B}(n,\alpha)$  and  $^{235}\text{U}(n,f)$  standard reactions [16], respectively. The first two detectors were in place during the  $^{241}\text{Am}(n,\gamma)$  measurement. The spatial distribution of the neutron beam at the irradiation position can be approximated by a two-dimensional (2D) Gaussian distribution with  $\sigma_x = \sigma_y = 0.62$  cm and does not vary significantly in the studied energy range [17,18]. The TOF response function, described in Ref. [7], is not very different from the one of the n\_TOF Phase-I, whose more detailed description can be found in Ref. [19].

### B. The detection system

To detect the  $^{241}\text{Am}(n,\gamma)$  events we used the n\_TOF TAC [20]. This detector, shown in Fig. 1, consists of 40  $\text{BaF}_2$  crystals of 15 cm in length covering  $\sim 95\%$  of the solid angle and is used to detect in coincidence (nearly) all the  $\gamma$  rays coming from the capture reactions. Each crystal is covered with two layers of 0.1-mm-thick Teflon foil and a 0.1-mm-thick polished aluminum sheet on the outside, to optimize the light collection. The crystals are also enclosed in 1-mm-thick  $^{10}\text{B}$  loaded carbon fiber capsules aimed at absorbing the scattered neutrons. Each of these capsules is coupled with an aluminum cylinder that houses a 12.7-cm Photonis XP4508B photomultiplier and a special voltage divider made at the Instituto Tecnológico e Nuclear in Lisbon that favors a fast signal recovery. The complete modules are attached to an aluminum honeycomb structure that holds the complete assembly. A neutron absorber made of borated polyethylene of 5- and 10-cm inner and outer radii, respectively, was placed in the center of the geometry, covering the inner surface of the TAC.

The intensity of the neutron beam was monitored during the entire  $^{241}\text{Am}(n,\gamma)$  campaign with the above-mentioned silicon flux monitor [13], which was mounted about 2 m upstream of

the sample. This detector was used to normalize the different measurements to their total neutron beam intensity and also to confirm the stability of the energy profile of the neutron beam.

The detector signals were recorded by a digital data acquisition system [21] based on Acqiris-DC270 digitizers with 8-bit resolution and operating most of the measurement at 250 MSamples/s, recording continuously for 32 ms for each neutron pulse, corresponding to a minimum neutron energy of 180 meV. Part of the measurement was performed with the digitizers operating at 500 MSamples/s, thus recording for 16 ms, corresponding to a minimum neutron energy of 0.7 eV. The data buffers were analyzed offline with dedicated pulse shape reconstruction algorithms. The algorithm used to analyze the  $\text{BaF}_2$  signals returns for each signal the TOF, the area, and other parameters used to distinguish the detected particle type:  $\gamma$  or  $\alpha$  (the latter is produced by the decay of Ra impurities in the crystals). The algorithm is described in detail in Ref. [22], and a more accessible reference of a similar routine is Ref. [23].

Each  $\text{BaF}_2$  detector was calibrated in energy from measurements performed with standard  $\gamma$ -ray sources ( $^{137}\text{Cs}$ ,  $^{88}\text{Y}$ , and  $\text{Am/Be}$ ), and the gain drifts were monitored throughout the entire measurement with the position of peaks due to the detection of  $\alpha$  particles. An energy threshold of 300 keV was applied to each  $\text{BaF}_2$  detector. This corresponds to the lowest value for which the energy calibration spectra were successfully reproduced by Monte Carlo simulations. The individual signals were grouped into TAC events using a coincidence window of 20 ns. Each TAC event is characterized by its TOF, total deposited energy ( $E_{\text{sum}}$ ) and crystal multiplicity ( $m_{\text{cr}}$ ), which is the number of detectors contributing to an event. The  $E_{\text{sum}}$  and  $m_{\text{cr}}$  values are used to apply cuts to the detected events in order to improve the capture-to-background ratio. In this paper, the word *event* always refers to these TAC events.

### C. The $^{241}\text{Am}$ and auxiliary samples and measurements

Thin powder samples of actinide oxides suffer from inhomogeneities [24–26] which can affect the resonance integrals (convolution with the neutron beam and self-shielding) and shape (due to self-shielding effects). For this reason, we took advantage of the technique developed at the Institute for Transuranium Elements (JRC-ITU) in Karlsruhe for producing homogeneous samples of actinide oxides mixed with an inert matrix. The sample was part of a set of 11  $^{241}\text{Am}$  samples produced by the JRC-ITU [27] for neutron total [5], capture [4,5], and  $(n,2n)$  [28] cross section measurements. Ten of these samples used  $\text{Al}_2\text{O}_3$  as inert matrix and the other one used  $\text{Y}_2\text{O}_3$ . Both Y and Al materials have similar properties from the neutronic point of view but for measuring above 1 keV Al has the advantage that resonances start at higher energies. The sample used for this experiment was made of 36.5 mg of  $^{241}\text{AmO}_2$  infiltrated into a 305-mg  $\text{Al}_2\text{O}_3$  matrix.

The fabrication procedure was as follows. Very small (10- to 100- $\mu\text{m}$ ) and porous alumina beads were introduced into a solution of the actinide in nitric acid. After some time, the beads absorbed a certain amount of actinide nitrates. Then the beads were dried and calcined, leading to a disperse mixture of  $\text{AmO}_2$  inside the inert matrix. The powder was

TABLE I. Number of pulses and total number of counts in the silicon flux monitor dedicated to each measurement.

Measurement	No. pulses	No. SiMon counts
$^{241}\text{Am}$	$1.41 \times 10^5$	$2.26 \times 10^7$
Dummy sample	$2.63 \times 10^4$	$3.39 \times 10^7$
Al canning	$3.27 \times 10^4$	$1.71 \times 10^7$
No sample	$2.88 \times 10^4$	$4.43 \times 10^6$
Graphite	$2.86 \times 10^3$	$3.42 \times 10^6$
$^{241}\text{Am}$ , beam off	$4.32 \times 10^3$	
No sample, beam off	$5.85 \times 10^3$	
$^{197}\text{Au}$	$1.09 \times 10^4$	$7.81 \times 10^6$

then pressed into a pellet of 342 mg and 12.26 mm in diameter for ensuring the mechanical stability, and encapsulated inside a 0.5-mm-thick Al canning. The mixture obtained in this way is very homogeneous, as it has been confirmed by different characterization techniques such as nondestructive x-ray radiographies or destructive  $\alpha$ -particle autoradiographies, performed on slices of the pellets during the development of the methodology.

The  $^{241}\text{Am}$  mass of the sample used in this work was 32.23(19) mg. The total amount of  $^{241}\text{Am}$  was determined by calorimetry at JRC Karlsruhe. The rest of the  $^{241}\text{Am}$  samples were prepared in a similar way, but with different  $^{241}\text{Am}$  contents. The masses of seven of these samples, none of them used in this work, were also measured at the JRC-Ispra [29], finding an excellent agreement with the measurements of the mass performed at JRC-ITU. Concerning impurities present in the sample, we detected  $^{237}\text{Np}$  ( $\sim 0.9$  mg) and  $^{240}\text{Pu}$  ( $\sim 0.016$  mg) during the resonance analysis. For the analysis the measured room temperature,  $296 \pm 3$  K, was taken as sample temperature.

The sample was placed in the center of the TAC, glued on a 50- $\mu\text{m}$ -thick kapton foil mounted in an aluminum ring with a diameter larger than the neutron beam. Due to the high sample activity ( $\sim 4$  GBq), a 2-mm-thick Pb layer was placed around the neutron beam at the position of the sample in order to strongly reduce the amount of  $\gamma$  rays originating in the sample decay and reaching the TAC.

To determine the background, additional measurements with other samples were carried out. The list of samples included a dummy sample including the Al canning plus the  $\text{Al}_2\text{O}_3$  matrix, the Al canning, and a graphite sample 12 mm in diameter and 6 mm thick, which is used to determine the TAC response to sample scattered neutrons. We also performed measurements without beam and without sample (no sample, beam off), without beam but with the sample in place ( $^{241}\text{Am}$ , beam off), and with neutron beam but without any sample. In addition, three  $^{197}\text{Au}$  samples were measured for normalization purposes. The number of pulses and total number of counts in the silicon flux monitor allocated to each of these measurements are summarized in Table I.

### III. DATA REDUCTION

The data reduction process is similar to the one applied for previous measurements performed with the TAC [30–32].

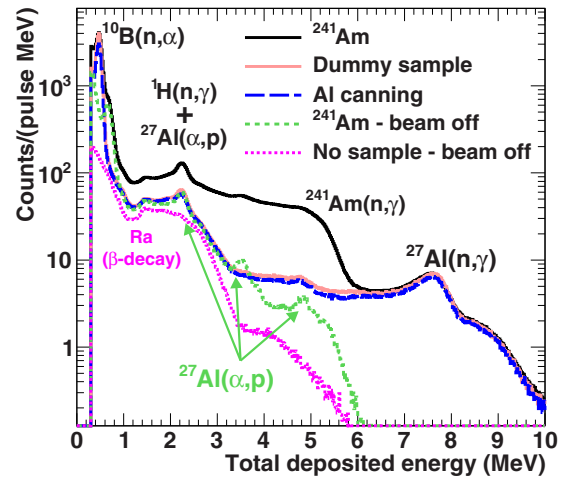


FIG. 2. Total deposited energy in the TAC during the  $^{241}\text{Am}(n, \gamma)$  and different background measurements. The data correspond to neutron energies between 1 and 10 eV and no cuts on  $m_{\text{cr}}$  have been applied to the detected events.

The capture yield is the fraction of incident neutrons that induce a  $(n, \gamma)$  reaction and can be determined experimentally as

$$Y_{n, \gamma}(E_n) = \frac{C_{\text{tot}}(E_n) - C_{\text{bkg}}(E_n)}{\varepsilon(E_n)\phi(E_n)}, \quad (1)$$

where  $E_n$  is the neutron energy,  $C_{\text{tot}}(E_n)$  and  $C_{\text{bkg}}(E_n)$  are the number of total and background counts registered by the TAC, respectively, under certain  $E_{\text{sum}}$  and  $m_{\text{cr}}$  cuts,  $\varepsilon(E_n)$  is the corresponding detection efficiency, and  $\phi(E_n)$  is the intensity of the neutron beam intercepted by the sample.

#### A. Background and selection of cuts in the detected events

Background events in the  $^{241}\text{Am}(n, \gamma)$  measurement can be attributed to two contributions: (i) events coming from neutron reactions in the  $^{241}\text{Am}$  nuclei, i.e., fission and elastic scattering, and (ii) the rest of the background, which results from the environmental background, the activity of the  $\text{BaF}_2$  crystals, the sample activity, and the interaction of the neutron beam with all the materials except the  $^{241}\text{Am}$  nuclei.

The latter contribution could be, in principle, obtained directly from the different background measurements summarized in Table I. The response of the TAC resulting from some of these measurements together with the one from a measurement with the  $^{241}\text{Am}$  sample, in terms of total deposited energy  $E_{\text{sum}}$ , is presented in Fig. 2. A maximum deposited energy from  $^{241}\text{Am}(n, \gamma)$  cascades is just above the neutron separation energy of  $^{242}\text{Am}$ ,  $S_n(^{242}\text{Am}) = 5.5$  MeV. Other visible contributions are the  $^{27}\text{Al}(n, \gamma)$  reaction, with  $S_n(^{28}\text{Al}) = 7.7$  MeV, and the  $(n, \gamma)$  and  $(n, \alpha)$  reactions in  $^1\text{H}$  and  $^{10}\text{B}$ , respectively. The difference between the two measurements performed without the neutron beam is due to the sample activity, whose main contribution above 1 MeV is due to the interaction of the  $\alpha$  particles coming from the decay of the  $^{241}\text{Am}$  with the  $^{27}\text{Al}$  of the  $\text{Al}_2\text{O}_3$  matrix [33].

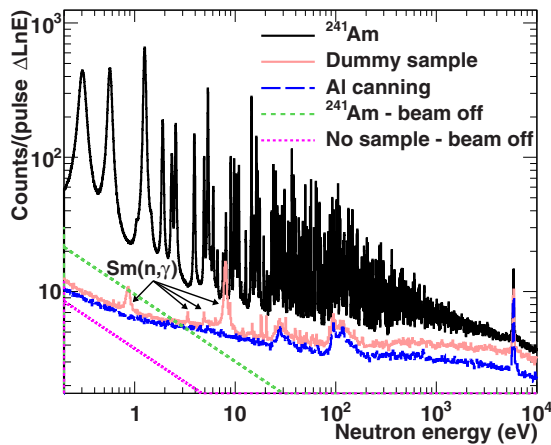


FIG. 3. Number of events detected per pulse and per unit lethargy ( $\Delta \ln E$ , which means that the bin contents have been divided by the natural logarithm of the ratio between the upper and lower bin limits) in the  $^{241}\text{Am}(n, \gamma)$  measurement as a function of the neutron energy, together with different background measurements. Only  $m_{\text{cr}} > 1$  and  $2.5 < E_{\text{sum}} < 6$  MeV events are shown.

From Fig. 2 it is easy to see that the capture-to-background ratio is significantly improved if the low ( $E_{\text{sum}} < 1$  MeV) and high ( $E_{\text{sum}} > 6$  MeV) energy events are excluded from the analysis. This holds also for restrictions on  $m_{\text{cr}}$ , because capture events have higher average multiplicity than the background ones. However, the more restricted the cuts are, the lower the detection efficiency becomes. In addition, there are pile-up effects induced by the high background counting rate which affect the detection of the capture signals (Sec. III B), and the more restricted the cuts are, the more important these effects become. A detailed analysis led to the optimum cuts of  $m_{\text{cr}} > 2$  and  $2.5 < E_{\text{sum}} < 6$  MeV, which were adopted in the present analysis. However, the capture yield has also been obtained for five additional combinations of cuts:  $2.5 < E_{\text{sum}} < 6$  MeV and  $3 < E_{\text{sum}} < 5$  MeV, combined with  $m_{\text{cr}} > 0$ ,  $m_{\text{cr}} > 1$ , and  $m_{\text{cr}} > 2$ . The differences between the six different yields were used to estimate uncertainties due to systematic effects in the results.

The number of events detected per proton pulse for the same measurements as in Fig. 2, but with additional cuts in  $E_{\text{sum}}$  and  $m_{\text{cr}}$ , are presented in Fig. 3 as a function of neutron energy. The difference between the measurements performed with the dummy and the Al canning samples should show only the effect of the interaction of the neutron beam with the  $\text{Al}_2\text{O}_3$  matrix. However, the results in Fig. 3 reveal that an unexpected resonant behavior appears in the spectrum of the dummy sample. These resonances are due to Sm contamination. This contamination most likely comes from a glue used to repair the dummy sample, since it broke down before this  $^{241}\text{Am}(n, \gamma)$  measurement was performed. Owing to this Sm contamination the background contribution of the  $\text{Al}_2\text{O}_3$  matrix could not be deduced directly from the dedicated background measurements, and some corrections which are described below were needed.

The background components due to the Al canning and  $\text{Al}_2\text{O}_3$  matrix both have two components related to capture

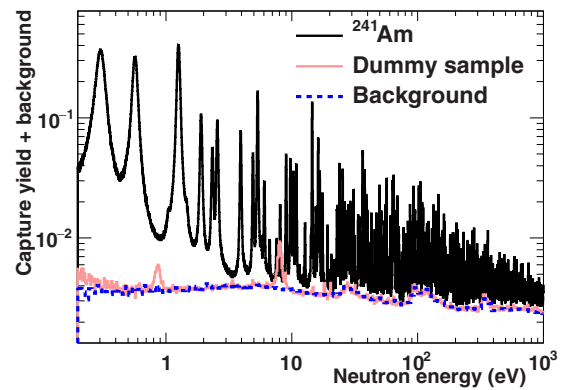


FIG. 4. Experimental  $^{241}\text{Am}(n, \gamma)$  yield (non-background-subtracted) together with the calculated background, in blue, and the background obtained if the Sm impurities are not removed, in red.

and neutron elastic scattering reactions in Al. The capture components are proportional to energy dependence of the  $\text{Al}(n, \gamma)$  cross section, which at neutron energies of our interest is in first approximation proportional to the inverse of the neutron speed, i.e.,  $E_n^{-1/2}$ . The elastic components should have the same neutron energy dependence for both materials. From these assumptions it follows that  $B_{\text{Al}_2\text{O}_3}(E_n) = \alpha E_n^{-1/2} + \beta B_{\text{Alcanning}}(E_n)$ , where  $\alpha$  and  $\beta$  are constants and  $B_{\text{Al}_2\text{O}_3}$  and  $B_{\text{Alcanning}}$  are the background components related to the interaction of the neutron beam with the  $\text{Al}_2\text{O}_3$  matrix and with the Al canning, respectively.  $B_{\text{Alcanning}}$  was easily obtained from the dedicated background measurements, and the  $\alpha$  and  $\beta$  parameters were obtained by fitting  $B_{\text{Al}_2\text{O}_3}(E_n) + B(\text{Sm})$  to reproduce the measurement performed with the dummy sample.  $B(\text{Sm})$  represents the contribution of the Sm impurities, which was deduced from the  $\text{Sm}(n, \gamma)$  cross sections taken from the evaluated libraries. The resulting background is presented in Fig. 4. We used the background calculated in this way only up to 80 eV, where the influence of Sm impurities is quite strong in the resonance peaks and negligible in the valleys. Above 80 eV the contribution of the Sm is below 1%, so we took the background calculated from the dummy sample measurement, after subtracting the Sm contribution.

The background related to elastic and fission reactions in the  $^{241}\text{Am}$  nuclei was estimated from the evaluated cross sections and the probability of detecting a scattered neutron and a fission reaction. The former probability, which depends on the neutron energy and on the  $E_{\text{sum}}$  and  $m_{\text{cr}}$  cuts, was obtained from the graphite sample measurement, under the assumption that the response of the TAC to neutrons scattered in carbon does not differ much from the response to neutrons scattered in  $^{241}\text{Am}$ . The probability of detecting a  $^{241}\text{Am}(n, f)$  event was assumed to be similar to the probability of detecting a  $^{235}\text{U}(n, f)$  event, which was determined in a  $^{235}\text{U}(n, \gamma)$  measurement performed with the n\_TOF TAC and a fission tagging detector [34]. Both contributions are very low in the energy range of interest and none of them introduces a sizable uncertainty in the measured  $^{241}\text{Am}(n, \gamma)$  cross section. In particular, the fission cross section of  $^{241}\text{Am}$  is about 200 times lower than the capture cross section. The background due to the elastically scattered neutrons is also very low—less than 1% with respect

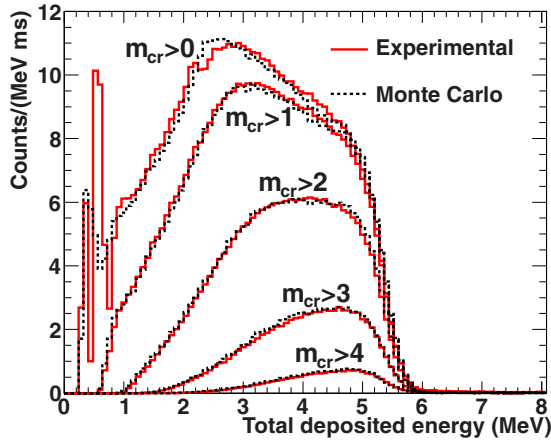


FIG. 5. Experimental (solid lines) and simulated (dotted lines) deposited energy spectra from  $^{241}\text{Am}$  capture cascades for different  $m_{\text{cr}}$  cuts. The experimental data were obtained from the strong  $^{241}\text{Am}$  resonance at  $\sim 0.3$  eV.

to the capture reactions in the neutron energy range of interest for  $m_{\text{cr}} > 1$  or  $m_{\text{cr}} > 2$  cuts. For  $m_{\text{cr}} > 0$  the contribution is smaller than 1% only below 1 keV, and goes up to 2.5% at 10 keV.

### B. Detection efficiency

The detection efficiency has been calculated from Monte Carlo simulations. The capture  $\gamma$ -ray cascades were generated with the DECAyGEN code [35], and transported into the TAC geometry (see Fig. 1) with a code based on the GEANT4 toolkit [36,37]. The results of the Monte Carlo code were then reconstructed in the same way as in the real experiment, including all the experimental effects such as the energy resolution of the crystals or the pile-up effects. The capture cascades generated by DECAyGEN depend on statistical models for the description of the level densities and photon strength functions. These models depend on some parameters, which were adjusted to reproduce the experimental deposited energy distributions for various  $m_{\text{cr}}$  cuts. The quality of the results is illustrated in Fig. 5. A detailed description of the entire process is given in Ref. [38], and the method was also used in Refs. [31,32].

We did not find any significant difference in the shape of the deposited energy spectra among several resonances (Fig. 6), and thus it was assumed that the detection efficiency depends only on the applied cuts for  $E_{\text{sum}}$  and  $m_{\text{cr}}$  and not on the energy of the captured neutron. In addition, we know from previous works [38] that sizable differences in the  $E_{\text{sum}}$  distributions lead to very small variations in the reconstructed efficiency. There is, however, a dependence of the detection efficiency on the TOF via pile-up effects, which are described below. The calculated efficiency values for the six different cuts used in this analysis are presented in Table II.

For the estimation of the uncertainties in the detection efficiencies two main components were considered, as described in Refs. [38–40]: one related to the generation of capture cascades and other related to the uncertainties of the TAC

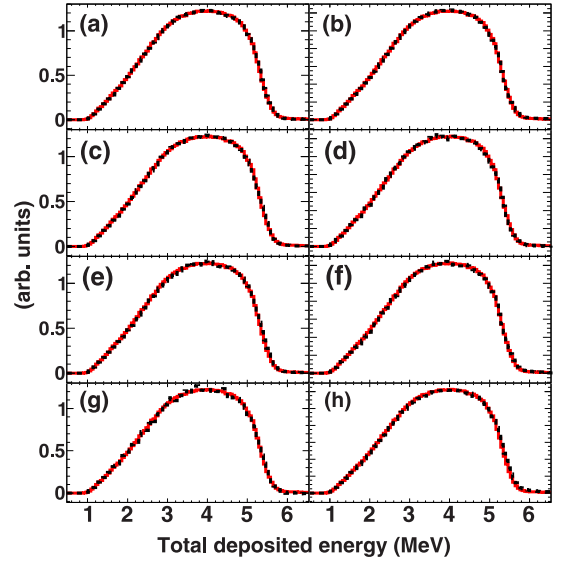


FIG. 6. Deposited energy spectra (with  $m_{\text{cr}} > 2$ ) from  $^{241}\text{Am}$  capture cascades for different resonances. The spectrum corresponding to the first resonance at 0.3 eV (solid lines) is compared to the spectra of the next eight resonances (dotted lines) at (a) 0.6, (b) 1.3, (c) 1.9, (d) 2.4, (e) 2.6, (f) 4.0, (g) 5.0, and (h) 5.4 eV. All the spectra have been normalized to the area.

geometry. The first component was estimated by performing multiple simulations with different EM deexcitation patterns for the capture cascades and observing when the simulated spectra deviate from the experimental data. The second component was estimated by varying the geometry parameters and calculating the impact of such variations on the detection efficiencies.

Concerning the pile-up effects, two different situations were considered. The first one is related to the high counting rate in the TAC due to capture cascades in the sample. This effect is very small ( $\lesssim 1\%$ ) for the  $^{241}\text{Am}(n, \gamma)$  cascades; however, it must be corrected for in the 4.9 eV saturated resonance of  $^{197}\text{Au}$ , which is used for normalization (see Sec. III C). To correct for these pile-up effects we used the third method described and validated in Ref. [41].

TABLE II. Calculated capture detection efficiencies for the six different cuts in  $E_{\text{sum}}$  and  $m_{\text{cr}}$  considered in this work. The right-hand column shows the calculated-to-experimental ratio of the integrals of the deposited energy histograms shown in Fig. 5, normalized to the cuts of  $2.5 < E_{\text{sum}} < 6$  MeV and  $m_{\text{cr}} > 0$ .

Cuts	Efficiency (%)	Calc./Expt.
$2.5 < E_{\text{sum}} < 6.0$ MeV, $m_{\text{cr}} > 0$	61.1(9)	1
$2.5 < E_{\text{sum}} < 6.0$ MeV, $m_{\text{cr}} > 1$	56.7(9)	0.996
$2.5 < E_{\text{sum}} < 6.0$ MeV, $m_{\text{cr}} > 2$	36.5(7)	0.989
$3.0 < E_{\text{sum}} < 5.0$ MeV, $m_{\text{cr}} > 0$	42.1(8)	1.013
$3.0 < E_{\text{sum}} < 5.0$ MeV, $m_{\text{cr}} > 1$	39.8(8)	1.005
$3.0 < E_{\text{sum}} < 5.0$ MeV, $m_{\text{cr}} > 2$	26.6(7)	0.995

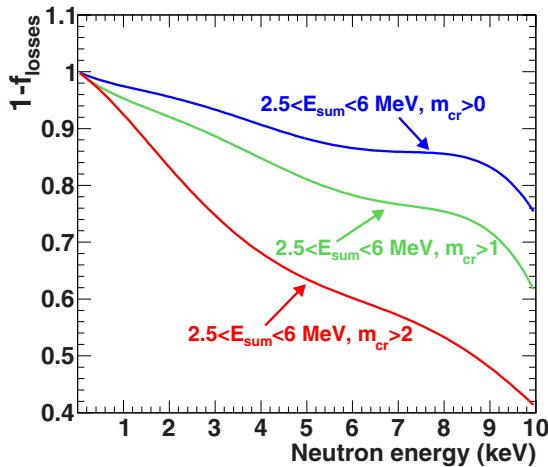


FIG. 7. One minus the fraction of events lost ( $f_{\text{losses}}$ ) due to the pile-up induced by the background, as a function of the neutron energy and for three different  $E_{\text{sum}}$  and  $m_{\text{cr}}$  cuts.

The second pile-up effect is induced by the high counting rate due to the background related to the neutron beam, which is a function of TOF and is the dominant component of the background except at the lowest neutron energies. When this counting rate becomes high enough (hundreds of counts per millisecond) then the background signals pile up with capture signals, thus modifying the probability of detecting them. We developed a new method of correcting for this effect which is based on the same methodology as in Ref. [41], i.e., in the offline manipulation of the digitized signals. In this case we copied the digitized signals obtained at low neutron energies (i.e., detected under a low background counting rate, with negligible pile-up) to a different TOF position in the digitized data buffer, corresponding to higher neutron energies and thus with higher background counting rates. The resulting artificially created data buffers were analyzed afterwards with the pulse shape reconstruction algorithms used for the standard analysis of the experiment. By comparing the results of the analyses obtained for the same signal but placed in different TOF positions in the digitized data buffers, it is possible to characterize the pile-up effects due to the background. This methodology will be described in more detail in a future publication [42].

The corrections of the capture yields due to this effect for three of the six different  $E_{\text{sum}}$  and  $m_{\text{cr}}$  cuts are presented in Fig. 7 as a function of the neutron energy. As shown, the more restrictive the cuts in  $E_{\text{sum}}$  and  $m_{\text{cr}}$  applied to the detected events are, the higher is the fraction of events lost due to the background induced pile-up.

### C. Normalization

The measurement was normalized by means of the saturated resonance method [43] to the strongest  $^{197}\text{Au}$  resonance at 4.9 eV. For this purpose we used three different  $^{197}\text{Au}$  samples, two of them with different thicknesses (250 and 50  $\mu\text{m}$ ) and with the same diameter as the  $^{241}\text{Am}$  sample (12.2 mm), and a third one with 50  $\mu\text{m}$  thickness and a larger diameter

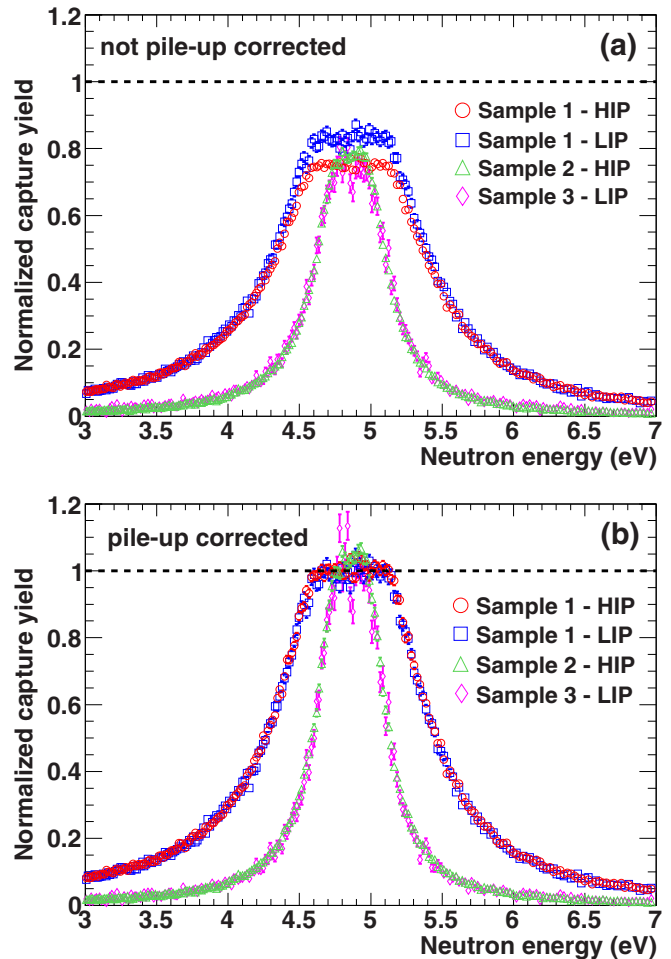


FIG. 8. (b) The experimental  $^{197}\text{Au}(n,\gamma)$  yields obtained for the three different samples, sample 1 (250  $\mu\text{m}$  thick, 12.2 mm diameter), sample 2 (50  $\mu\text{m}$  thick, 12.2 mm diameter), and sample 3 (50  $\mu\text{m}$  thick, 45 mm diameter), and the two beam pulse intensities, high (HIP) and low (LIP). The yields have been normalized to reproduce the results obtained from SAMMY using JEFF-3.2. (a) The same experimental data without performing pile-up corrections.

covering the entire neutron beam. The three  $^{197}\text{Au}$  samples were measured with the nominal neutron beam intensity and also with an intensity 2.3 times smaller. The comparison with different count rates validated the pulse pile-up corrections, as shown in Fig. 8. The measurement performed with the third  $^{197}\text{Au}$  sample cannot be directly used to normalize, since it has a different diameter than the  $^{241}\text{Am}$  sample. However, it can be included in the comparison and used to validate the pile-up corrections after re-normalizing it to the measurement performed with the sample with the same thickness but smaller radius. This renormalization was performed in the tail of the  $^{197}\text{Au}$  resonance, where no pulse pile-up corrections are needed.

In Table III we present the normalization factors obtained from the different  $^{197}\text{Au}$  measurements. In all the cases we used the measurement performed with the thicker  $^{197}\text{Au}$  sample (sample 1) and with low intensity pulses to normalize the yields. Each of these normalization factors was obtained for



TABLE III. Normalization factors obtained by means of the saturated resonance method using three different  $^{197}\text{Au}$  samples and two different beam intensities.

	$^{197}\text{Au}$ sample		High intensity pulses	Low intensity pulses
	Thickness ( $\mu\text{m}$ )	Diameter (mm)		
Sample 1	250	12.20	0.986(8)	1.000(9)
Sample 2	50	12.20	0.969(10)	0.975(11)
Sample 3	50	45.00		0.968(8)

different  $E_{\text{sum}}$  and  $m_{\text{cr}}$  cuts. The values and uncertainties in Table III are the mean and the standard deviation of the results of each case, respectively. All the normalization factors are compatible within two standard deviations. The measurement performed with the nominal neutron beam intensity and the largest diameter  $^{197}\text{Au}$  sample was not used because the pile-up correction method cannot handle the instantaneous counting rate as high as about four events per microsecond.

The uncertainty in the normalization was estimated taking into account both the spread of the values and the uncertainties in Table III, obtaining an uncertainty of 1.5%. To this value we added the uncertainty due to the  $^{197}\text{Au}(n,\gamma)$  detection efficiency. As for  $^{241}\text{Am}$ , it is estimated from the uncertainties associated with the generation of capture cascades (0.7% for  $^{197}\text{Au}$ ) and of the simulated TAC geometry. However, the uncertainty due to the TAC geometry was not added in this case since it was already included in the uncertainty of the  $^{241}\text{Am}(n,\gamma)$  detection efficiency, and it propagates in the same way, introducing a strong correlation between both detection efficiencies. If we make a quadratic sum of both quantities we obtain a total uncertainty of 1.7% in the normalization to the saturated resonance of  $^{197}\text{Au}$ .

#### D. Uncertainties

The uncertainties due to systematic effects in the capture yield were estimated in the following way. The quantities with larger uncertainties which affect the normalization process are the detection efficiency (2%), the normalization to the saturated resonance of  $^{197}\text{Au}$  discussed in the previous section (1.7%), and the sample mass (0.6%). If we make a quadratic sum of these quantities we obtain a total normalization uncertainty of 2.7%.

In addition to the normalization uncertainty we have to consider the energy dependent uncertainty on the neutron fluence shape, which is 1% below 100 eV and 2% between 100 eV and 10 keV [12].

Other sources of uncertainty come from the determination of the background and from the pile-up corrections. We estimated the uncertainty due to both these effects at the same time from the differences between the resulting capture yields obtained with the different  $E_{\text{sum}}$  and  $m_{\text{cr}}$  cuts. In particular, we estimated it as the standard deviation calculated from the six different resulting yields. The result is presented in Fig. 9, as a function of neutron energy, together with the corresponding relative uncertainties due to counting statistics. Note that the size of the latter depends largely on the width of the neutron

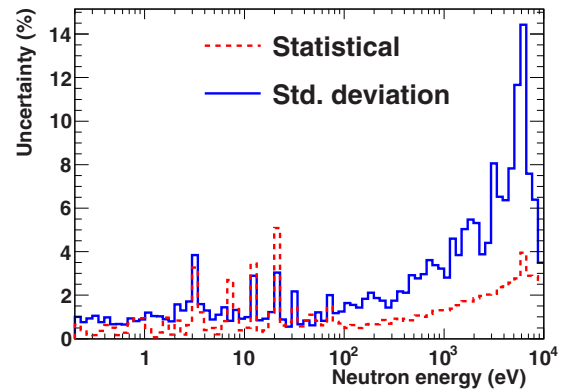


FIG. 9. Standard deviation of the capture yield obtained from the six different  $E_{\text{sum}}$  and  $m_{\text{cr}}$  cuts mentioned in the text as a function of the neutron energy, together with the uncertainties due to counting statistics.

energy intervals considered, whereas this dependency is much smaller in the standard deviation. The increase of the values at  $\sim 6$  keV is due to the first  $^{27}\text{Al}$  resonance.

## IV. CROSS SECTION ANALYSIS

### A. Analysis of the resolved resonance region

The resolved resonance region (RRR) was analyzed with the SAMMY code (version 8.0.0) [19]. In the most recent evaluated libraries the RRR extends up to 150–160 eV, but we performed a resonance analysis up to 700 eV. We have fitted, using the Reich-Moore approximation, the energy  $E_0$  and the neutron width  $\Gamma_n$  of each resonance, and the radiative capture width  $\Gamma_\gamma$  only when its uncertainty due to counting statistics was less than 10%. The resonance parameters of the negative resonances, the scattering radius, and all fission widths were taken from the JEFF-3.2 evaluation [44], after verifying that large variations of these parameters do not affect the resulting capture yield significantly. It was confirmed by the techniques described in Ref. [45] that all the resonances observed in the investigated energy range were  $s$ -wave resonances. As it was not possible to distinguish the total spin values  $J = 2, 3$ , only the  $g\Gamma_n$  values were determined, with  $g = \frac{(2J+1)}{(2I+1)(2j+1)}$ , where  $J$ ,  $I = 5/2$  and  $j = 1/2$  are the spins of the resonance, target nucleus, and neutron, respectively. The time-to-energy relation was obtained by adjusting the  $n_{\text{TOF}}$  time-of-flight effective distance to reproduce the energies of the resonances of  $^{197}\text{Au}$  in the JEFF-3.2 evaluation, yielding 185.59(2) m.

Note that above a certain energy we are not fitting individual resonances but clusters of resonances in many cases, since it is not possible to resolve them accurately. However, having a resonant description of the cross section up to higher energies is useful for more accurate self-shielding calculations.

Together with the  $^{241}\text{Am}$  resonances, we included in the SAMMY input the  $^{237}\text{Np}$  and  $^{240}\text{Pu}$  impurities and the  $^{16}\text{O}$  and  $^{27}\text{Al}$  of the  $\text{AmO}_2$  compound and the  $\text{Al}_2\text{O}_3$  matrix.  $^{16}\text{O}$  and  $^{27}\text{Al}$  were included only to properly calculate self-shielding and multiple scattering effects. Detection efficiency for their cascades was set to zero, since their contributions were included in the calculation of the background. Indeed,

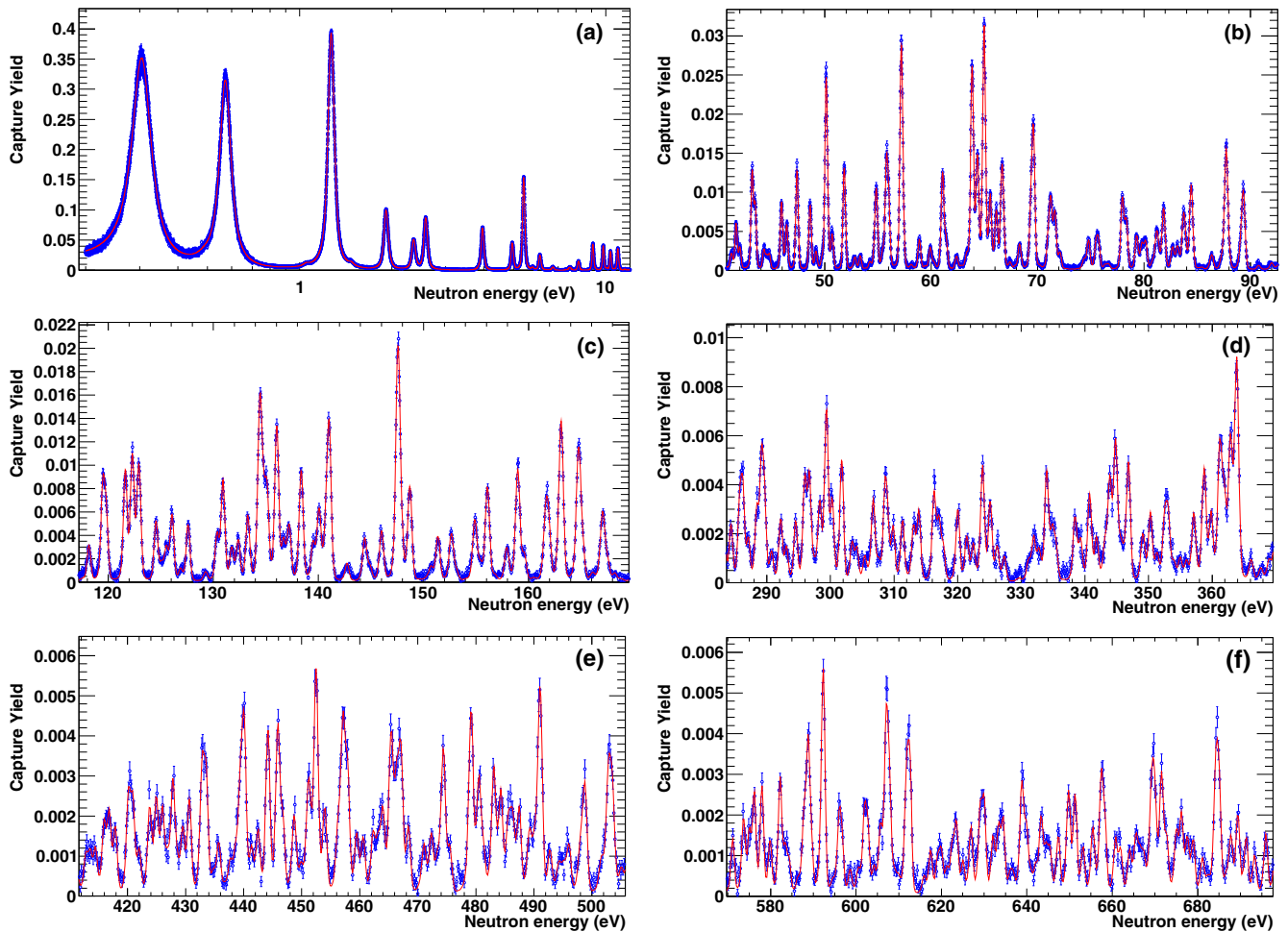


FIG. 10. Examples of the fitted  $n_{\text{TOF}}$  capture yield, in different energy ranges. The data points correspond to the experimental capture yield and the solid line to the fit performed with SAMMY.

we studied in detail the self-shielding and multiple scattering effects by comparing calculations performed with SAMMY, MCNP-6.1 [46], and GEANT4. In these calculations we obtained the theoretical capture yield under different conditions: with and without the Al canning, and with and without the  $\text{Al}_2\text{O}_3$  matrix. We found that the results obtained with the three codes are in a reasonable agreement, better than 0.5%. They showed that the effect of the Al canning is negligible; the effect of the  $\text{Al}_2\text{O}_3$  matrix introduces an increase in the number of detected capture events by  $\sim 1.5\%$ , nearly constantly in the energy range of interest, and that the self-shielding due to the  $^{241}\text{Am}$  itself is small ( $< 2\%$ ) except for the first three resonances, where it is around 10%. The  $n_{\text{TOF}}$  capture yield is presented together with the results of the SAMMY fit for several neutron energy ranges in Fig. 10.

We obtained the mean values of the resonance parameters and their uncertainties due to counting statistics from the SAMMY analysis performed with the optimum cuts of  $m_{\text{cr}} > 2$  and  $2.5 < E_{\text{sum}} < 6$  MeV, together with their correlations. Total uncertainty of the resonance parameters due to systematic effects is given by three contributions: (i) the uncertainties due to systematic effects of the experimental yield (Sec. III D),

(ii) the uncertainty in the temperature of the sample, and (iii) the uncertainty due to the Doppler broadening model used in the fitting procedure.

Concerning contribution (i), we performed independent resonance analysis for each of the six experimental data sets resulting from the different cuts mentioned before in order to take into account the contributions due to the determination of the background and due to the pile-up corrections. The uncertainty of each fitted parameter due to these two effects was estimated as the standard deviation of the different fitted values. An additional 2.7% normalization uncertainty was added to the  $g\Gamma_n$  parameters, since the area of each resonance is in good approximation proportional to  $g\Gamma_n$  when capture is the dominant reaction.

The last two contributions, (ii) and (iii), were estimated by performing fits with three different sample temperatures, 293, 296, and 299 K, and with two different Doppler broadening models, the free gas model (FGM) and the crystal-lattice model (CLM) [19]. In the latter case, we used the phonon spectrum of  $\text{UO}_2$  (SAMMY example file t124f.clm), since it has not been measured for  $\text{AmO}_2$ . In both cases the uncertainties of each fitted parameter were estimated as the standard deviation of the

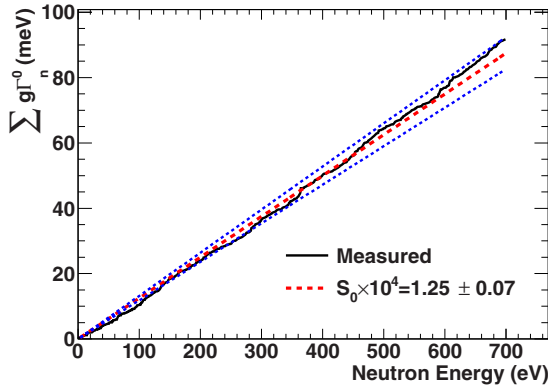


FIG. 11. Cumulative distributions of the neutron widths compared with the value of  $S_0$  obtained in this work. The two blue lines represent the uncertainty due to the number of resonances used in the determination of  $S_0$ .

different fitted values. The mean values were obtained using 296 K and the CLM for the Doppler broadening.

The values of the fitted resonance parameters are presented in Tables VI and VII. The  $\Gamma_\gamma$  values with uncertainties due to counting statistics larger than 10% were fixed to the average radiative capture width, which was calculated from the rest of the values. The quadratic sum of all the uncertainties due to systematic effects but the one due to the normalization are provided as well. Above 52 eV, all  $\Gamma_\gamma$  values were fixed to  $\langle \Gamma_{\gamma,0} \rangle = 45.4$  meV; thus only the energies and  $g\Gamma_n$  values are given in Table VII.

The average radiation width  $\langle \Gamma_{\gamma,0} \rangle$  was determined from the fitted values listed in Table VI. The resulting value was  $\langle \Gamma_{\gamma,0} \rangle = 45.4 \pm 0.2 \pm 1.1 \pm 0.4$  meV, where the uncertainties are, respectively, due to the uncertainties in the individual  $\Gamma_\gamma$  parameters due to the counting statistics, to Doppler broadening, and to the sample temperature. The rest of the contributions to uncertainties are negligible. The quadratic sum of all these uncertainties gives a final value of  $\langle \Gamma_{\gamma,0} \rangle = 45.4 \pm 1.2$  meV.

The neutron strength function for  $s$ -wave resonances  $S_0$  was obtained as  $S_0 = \sum_\lambda g \Gamma_{n,\lambda}^0 / \Delta E$  and  $\Delta S_0 / S_0 = \sqrt{2/N}$  [47], with  $\Delta E$  the width of the energy interval considered and  $N$  the number of resonances in this interval. The resulting value is  $S_0 \times 10^4 = 1.25 \pm 0.07 \pm 0.03 \pm 0.02$ , where the uncertainties are, respectively, due to the number of resonances used in the calculation, to the normalization, and to the remaining systematic effects of the capture yield. The quadratic sum of all these uncertainties gives a final value of  $S_0 \times 10^4 = 1.25 \pm 0.08$ . For the calculation of  $S_0$  we considered resonances only up to 400 eV, since the resonance analysis is less precise as the energy increases. However, the results obtained at higher energies are compatible within uncertainties, as presented in Fig. 11.

An estimation of the  $s$ -wave average level spacing  $D_0$  can be obtained, from  $D_0 = \Delta E / (N - 1)$  [47], where  $N$  is the number of resonances observed in the neutron energy interval between  $E_1$  and  $E_2$  and  $\Delta E = E_2 - E_1$ . However, the smallest resonances are usually not detected (missing resonances), and their number has to be estimated as well. This was done by assuming that the values of the reduced

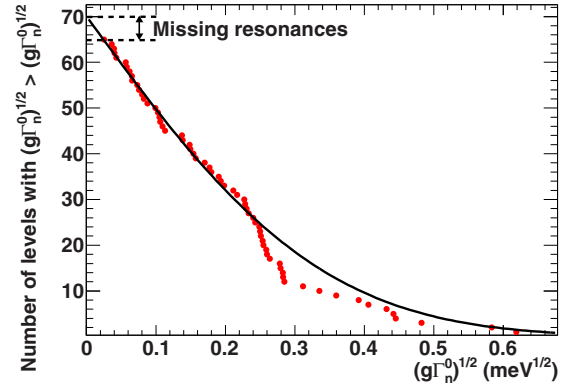


FIG. 12. Estimation of the number of missing resonances, in this case 8.5%, performed in the 0–40 eV energy range. The experimental points were fitted to Eq. (2).

neutron widths  $\Gamma_n^0 = \Gamma_n(E_0/1 \text{ eV})^{-1/2}$  are distributed, for each spin value  $J$ , according to the Porter-Thomas distribution  $p(x)dx = e^{-x^2} / \sqrt{2\pi x} dx$ , where  $x = \Gamma_{n,J}^0 / \langle \Gamma_{n,J}^0 \rangle$ . With some manipulations of the Porter-Thomas distribution [31], it follows that, for a given energy interval, the number of resonances with  $\sqrt{g\Gamma_n^0}$  greater than a certain value,  $x$ , can be obtained from

$$f(x) = \left( \frac{\Delta E}{D_0} + 1 \right) \frac{2}{\sqrt{\pi} \sqrt{2S_0 D_0}} \int_x^\infty \exp\left(-\frac{y^2}{2S_0 D_0}\right) dy. \quad (2)$$

This formula can be used to estimate the number of missing resonances by fitting the value of  $D_0$ , as it is presented in Fig. 12.

An alternative method we used was to generate by Monte Carlo several artificial resonance sequences from the values of  $S_0$  and  $\langle \Gamma_{\gamma,0} \rangle$  obtained in this work and different values of  $D_0$ . We used the same analysis procedure as in Ref. [48]. From the comparison of the simulations with the experimental results we obtained  $D_0 = 0.56 \pm 0.04$  eV, which is fully compatible with the values of  $D_0$  derived from the previous method.

## B. Analysis of the unresolved resonance region

The analysis of the unresolved resonance region (URR) was performed with the SAMMY code, which contains a modified version of the FITACS code [19,49], which uses Hauser-Feshbach theory [50] with width fluctuation corrections. To perform the analysis we used the capture cross section instead of the reaction yield, as it is required by SAMMY in the URR. As we mentioned in Sec. IV A, we studied in detail the self-shielding and multiple scattering effects in the sample by performing several Monte Carlo simulations. We concluded that above 150 eV the self-shielding and multiple scattering effects due to reactions in  $^{241}\text{Am}$  are negligible ( $<0.3\%$ ), and that the effect of the  $\text{Al}_2\text{O}_3$  matrix is an increase of the number of detected capture events by 1.5%. Thus, the cross section was obtained by dividing the capture yield by the sample thickness  $n$  and by 1.015:  $\langle \sigma_\gamma(E_n) \rangle = \langle Y_\gamma(E_n) \rangle / (n \times 1.015)$ .

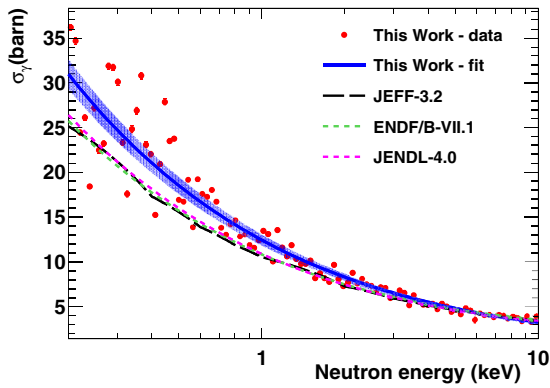


FIG. 13. Measured (markers) and fitted (solid line)  $n_{\text{TOF}}$  capture cross section in the URR. The uncertainty of  $S_0$  is shown as a shadowed area. The cross sections provided by the JEFF-3.2, ENDF/B-VII.1, and JENDL-4.0 evaluations, which are very similar, are also plotted.

The analysis of the URR was performed by fixing  $D_0$  and  $\langle \Gamma_{\gamma,0} \rangle$  to the values obtained from the statistical analysis of the RRR, since they cannot be determined with a reasonable accuracy from the URR, and by fitting  $S_0$ . The  $p$ -wave contribution starts to be more important at higher energies, and other parameters such as the channel radius or  $R_1^\infty$  cannot be determined from this measurement. The analysis was performed with the six different cuts in  $E_{\text{sum}}$  and  $m_{\text{cr}}$  mentioned above, and also considering different neutron energy ranges for the determination of  $S_0$ . This allowed us to estimate different sources of uncertainty.

The obtained value was  $S_0 \times 10^4 = 1.19 \pm 0.03 \pm 0.03 \pm 0.02 \pm 0.05$ , where the uncertainties are due to the normalization, to the sensitivity of the result to the neutron energy range chosen for the fit, to the uncertainties in  $D_0$  and  $\langle \Gamma_{\gamma,0} \rangle$ , and to the  $E_{\text{sum}}$  and  $m_{\text{cr}}$  cuts, respectively. The latest contribution represents mainly the uncertainty due to the pile-up corrections (Fig. 9). The uncertainty derived from counting statistics is negligible in this case. A quadratic sum of these uncertainties leads to a final value of  $S_0 \times 10^4 = 1.19 \pm 0.07$ , which is in a perfect agreement with the one obtained from the RRR,  $S_{0,\text{RRR}} \times 10^4 = 1.25 \pm 0.08$ .

The resulting fitted cross section in the URR is shown in Fig. 13, together with the values present in different evaluations. The differences between the cross sections in different evaluations are very small, but they differ significantly from the results of this work in the lower energy range. In particular, we obtained a cross section which is around 20% higher than the evaluated ones below 1 keV and which becomes compatible with them at a few keV.

## V. COMPARISON WITH PREVIOUS MEASUREMENTS AND EVALUATIONS

The TOF  $^{241}\text{Am}$  capture and transmission measurements performed up to now in the energy range of this measurement are listed in Table IV. In order to compare our results with the previous ones at low neutron energies we present in Fig. 14 the ratio between  $g\Gamma_n$  obtained in this work and that obtained in previous works and evaluations. At these energies the

TABLE IV. Time-of-flight transmission (T), capture (C), and absorption (A) measurements performed up to now.

Ref.	Type	Range (eV)
This work	C	0.2–( $1.0 \times 10^4$ )
Fraval <i>et al.</i> (2014) [4]	C	0.02–( $1.5 \times 10^5$ )
Harada <i>et al.</i> (2014) [51]	C	0.01–100
Lampoudis <i>et al.</i> (2011) [5]	C and T	0.02–110
Jandel <i>et al.</i> (2008) [52]	C	0.02–( $3.45 \times 10^5$ )
Vanpraet <i>et al.</i> (1986) [53]	C	0.69–( $1.5 \times 10^5$ )
Gayther <i>et al.</i> (1977) [54]	A	100–( $5 \times 10^5$ )
Weston and Todd (1976) [55]	A	0.01–( $3.77 \times 10^5$ )
Kalebin <i>et al.</i> (1976) [56]	T	0.004–30
Derrien and Lucas (1975) [57]	T	0.8–( $1 \times 10^3$ )
Slaughter <i>et al.</i> (1961) [58]	T	0.25–41.7
Adamchuk <i>et al.</i> (1955) [59]	T	0.006–82.1

capture reaction dominates over the other reaction channels (elastic scattering and fission) and these ratios correspond in good approximation to the capture cross section ratios (at resonances).

Figure 14 indicates that our results are in a reasonable agreement with those provided by Lampoudis *et al.*, especially if we consider the uncertainties due to normalization, which are 2.7% (this work) and 2.0% (Lampoudis *et al.* [5]). On the contrary, our results are between 10% and 40% higher than the ones provided by Fraval *et al.* [4], Jandel *et al.* [52], Kalebin *et al.* [56], and Derrien and Lucas [57].

The data from Weston and Todd [55] were normalized to an evaluated thermal  $^{241}\text{Am}(n,\gamma)$  cross section, so only the energy dependence of the cross section is comparable with our data. Slaughter *et al.* [58] also reported resonance parameters, but the uncertainties are so large that a comparison is not very informative.

The differences in data are reflected in the resonance parameters found in evaluated libraries. The evaluation present in JEFF-3.2 adopts essentially the results provided by Lampoudis

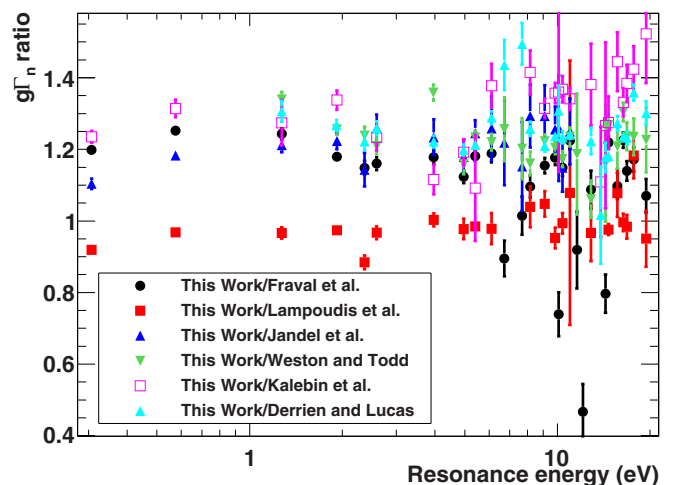


FIG. 14. Ratio of the  $g\Gamma_n$  obtained in this work and the ones obtained in previous measurements, in the low neutron energy range. Only uncertainties due to counting statistics have been considered.

TABLE V. Resonance integrals,  $I_0 = \int_{E_c}^{\infty} \sigma_{\gamma}(E)/EdE$  (in barn), provided by different experiments and evaluations. The horizontal lines separate TOF data and evaluations (top), direct measurements of  $I_0$  (center), and direct measurements of  $I_0^g$  only (bottom).

Ref.	$E_c$ (eV)			
	0.107	0.369	0.4	0.5
This work	3310(90) <sup>a</sup>	1938(50)	1889(49)	1792(47)
Fraval (2014) [4]	2891	1620	1578	1496
Jandel (2008) [52]	3124	1683	1637	1552
JEFF-3.2 [44]	3689	1972	1922	1826
JENDL-4.0 [62]	3261	1728	1681	1587
Shinohara (1997) [63]				1808(146)
				1694(146) <sup>b</sup>
Gavrilov (1976) [64]				1800(90)
				1570(10) <sup>b</sup>
Harbour (1973) [65]		1538(118)		
		1330(117) <sup>b</sup>		
Hellstrand (1970) [66]				2700 <sup>c</sup>
Bak (1967) [67]			2400(200)	
			2100(200) <sup>b</sup>	
Nakamura (2007) [68]	3500			
	(300) <sup>b</sup>			
Maidana (2001) [69]				1665(91) <sup>b</sup>
Deal (1964) [70]				900 <sup>b</sup>

<sup>a</sup>Extrapolated below 0.2 eV by using the resonance parameters obtained in this work and the negative resonances from JEFF-3.2.

<sup>b</sup>Value corresponds to  $I_0^g$  only, i.e., includes capture reactions leading to  $^{242g}\text{Am}$ .

<sup>c</sup> $E_c$  is 0.55 eV.

*et al.* in the RRR [60], whereas JENDL-4.0 takes those from Jandel *et al.* below 12 eV (multiplied by 1.029) and from an evaluation based mainly on the results reported by Derrien and Lucas above 12 eV. ENDF/B-VII.1 [61] adopted the JENDL-4.0 evaluation in the RRR.

Additional information concerning the capture cross section in the few-eV neutron energy range can be obtained from direct measurements of the resonance integral  $I_0$ ,  $I_0 = \int_{E_c}^{\infty} \sigma_{\gamma}(E)/EdE$ , with  $E_c$  usually being taken as 0.5 eV. In the case of the  $^{241}\text{Am}(n,\gamma)$  cross section the contribution of the first three resonances to  $I_0$  is  $\sim 75\%$ , whereas the value of the integral above 20 eV represents less than 10%, according to parameters from JEFF-3.2. The product from the  $^{241}\text{Am}(n,\gamma)$  reaction can be either the isomer ( $^{241m}\text{Am}$ ) or the ground state ( $^{241g}\text{Am}$ ). We can define the resonance integrals  $I_0^g$  and  $I_0^m$  feeding these states, respectively. The total resonance integral is given by  $I_0 = I_0^m + I_0^g$ . Depending on the experimental technique, the integral experiments provide either all three resonance integrals [63–65,67], the total resonance integral [66], or the resonance integral feeding the ground state [68–70].

The results from these integral measurements are listed in Table V, together with  $I_0$  values derived from TOF data. The uncertainties presented in the  $I_0$  values obtained in this work are due to the normalization (2.7%). This work and JEFF-3.2 (based on Lampoudis *et al.*) values are fully compatible with the values provided by Shinohara *et al.* and Gavrilov *et al.*, whereas the  $I_0$  from Fraval *et al.* and Jandel *et al.* are 15–20%

smaller. On the contrary, the last two are closer (only 5–10% larger) to Harbour *et al.* than this work and JEFF-3.2 results, which are 25% larger. The value from Hellstrand *et al.* does not seem to be compatible with any of the TOF measurements. The data from Bak *et al.* are 2.5 standard deviations larger than this work and JEFF-3.2 and more than three standard deviations larger than the rest of the TOF data.

The  $I_0^g$  cannot be directly compared with the TOF data. However, the result provided by Maidana *et al.* [69] is compatible with the data of Shinohara *et al.* and Gavrilov *et al.*, confirming them in a certain way. The value provided by Nakamura *et al.* [68] cannot be compared with any of the other integral measurements, since their value for  $E_c$  is 0.107 eV. To compare it with the TOF data we can scale it by the  $I_0/I_0^g$  factors from Shinohara *et al.* and Gavrilov *et al.*, obtaining 3700 and 4000 b, respectively. Both values are in good agreement with JEFF-3.2, and the lowest value also with this work and JENDL-4.0 (1.3 standard deviations). The values from Fraval *et al.* and Jandel *et al.* are 2.7 and 2.0 standard deviations below, respectively. Finally, the value of Deal *et al.* [70] is not compatible with any other measurement.

In order to extend the comparison to higher energies we compare the ratios of our and previously published cross sections in Fig. 15. Presented error bars correspond only to uncertainties due to counting statistics in all cases but Jandel *et al.*, where uncertainties due to systematic effects are also included. For a correct interpretation of Fig. 15 the uncertainties due to systematic effects have to be considered as well. In our case, in addition to the 2.7% normalization uncertainty, there is an extra 4–8% uncertainty in the keV energy region (Fig. 9). The conclusions that can be drawn are the following:

- (1) The results reported by Fraval *et al.* are not compatible with ours. Note that both results were obtained from measurements performed with the same sample and at the same facility, but using different detection methods.
- (2) Harada *et al.* measured only the shape of the  $^{241}\text{Am}(n,\gamma)$  cross section up to 100 eV, and it seems to be compatible with our results. Data represented in Fig. 15, taken from Ref. [71], are normalized to the JENDL-4.0 thermal cross section (684 b). If we renormalize them to the thermal cross section provided by JEFF-3.2 (747 b) our and Harada *et al.*'s cross sections are compatible both in shape and in absolute value. A recent measurement of the  $^{241}\text{Am}(n,\gamma)$  thermal cross section performed in the Minerve reactor [72] seems to confirm the value from JEFF-3.2. There is also a recent work which reviews previous thermal cross section measurements [73], and gives the value of 720(14) b.
- (3) The cross section from Jandel *et al.* has a similar shape to ours below 1 keV, but is 15% smaller. Above 1 keV, both results are quite compatible.
- (4) The cross sections from Vanpraet *et al.* and Weston and Todd are not compatible with ours, either in shape or in absolute value below around 0.5 keV. On the contrary, above 0.5–1 keV the three cross sections are compatible.

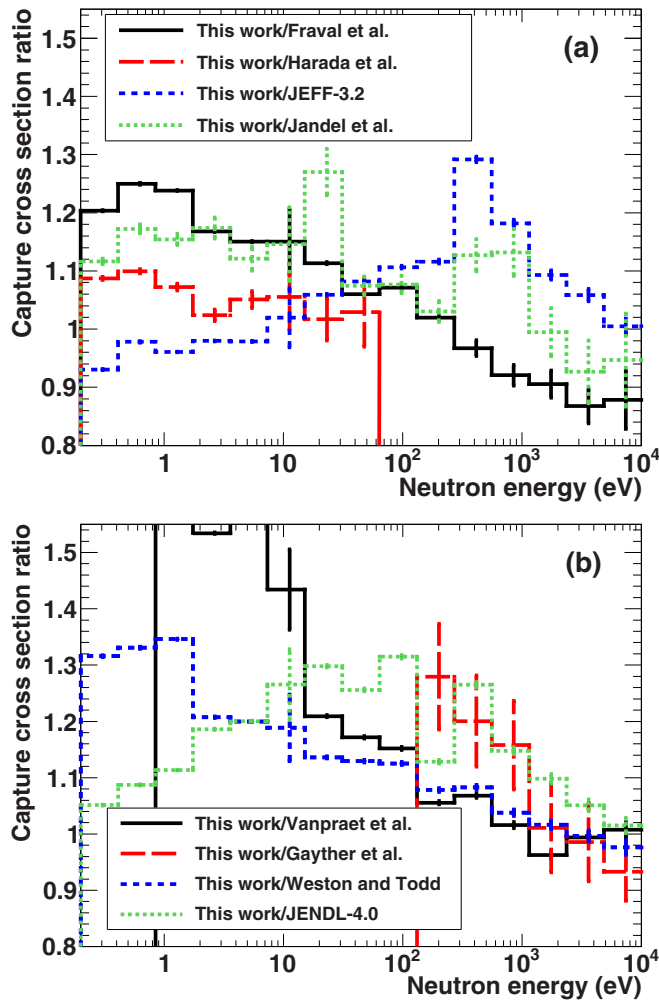


FIG. 15. Ratio between the capture cross section ( $\int_{E_1}^{E_2} \sigma(E)dE$ ) obtained in this work and the ones obtained in previous measurements and evaluations. Only uncertainties due to counting statistics have been considered in all cases but Jandel *et al.*, where uncertainties due to systematic effects are also included.

- (5) The uncertainties in the cross section from Gayther *et al.* are very large, but it seems clear that the shape of the cross section is different than ours.
- (6) The cross section from JEFF-3.2, which adopts mainly the results from Lampoudis *et al.* below 100 eV, is quite compatible in absolute value with our results at low neutron energies. However, there are sizable differences in the shape: at 0.2 eV our results are 7% lower, at 10 eV they are similar, and at 150 eV our results are 12% higher. Above 160 eV, i.e., in the URR in the evaluation, the trend goes in the opposite direction: the results of this work are 30% higher at 300 eV and the disagreement gradually decreases with the neutron energy, being compatible above 5 keV.
- (7) The cross section from JENDL-4.0, which was adopted in ENDF/B-VII.1 in the RRR, below 150 eV, and very similar in the URR, is not so different from ours at the lowest and highest energies. However, it differs up to 30% at intermediate neutron energies.

## VI. CONCLUSIONS

The  $^{241}\text{Am}$  neutron capture cross section was measured at n\_TOF using the segmented BaF<sub>2</sub> Total Absorption Calorimeter in the energy range between 0.2 eV and 10 keV. The uncertainties due to counting statistics in the resulting capture yield are relatively small. The uncertainties due to systematic effects are 2.7% due to the normalization plus, on average, around 1% below 100 eV, around 2–3% between 100 eV and 1 keV, and around 4–8% between 1 and 10 keV, due to the pile-up corrections and the determination of the background.

A resolved resonance analysis was performed on the resulting capture yield up to 700 eV, which is significantly higher than 150–160 eV, the upper limit of the RRR of the present evaluated libraries. This allows a more precise description of the cross section useful for more accurate self-shielding calculations. Statistical analysis of resonance parameters yielded  $\langle \Gamma_{\gamma,0} \rangle = 45.4 \pm 1.2$  meV,  $D_0 = 0.56 \pm 0.04$  eV, and  $S_{0,\text{RRR}} \times 10^4 = 1.25 \pm 0.08$ .

The cross section obtained at higher energies, in the URR, is fully consistent with the predictions based on these average resonance parameters, thus obtaining a consistent description of the cross section in the full neutron energy range under study. In particular, by fixing the  $\langle \Gamma_{\gamma,0} \rangle$  and  $D_0$  to the values obtained from the RRR we obtained a neutron strength function  $S_{0,\text{URR}} \times 10^4 = 1.19 \pm 0.07$ .

At low neutron energies our results are in reasonable agreement with the ones obtained by Lampoudis *et al.*, adopted by JEFF-3.2, and differ by around 20% from other experimental data [4,52,56,57]. Our results are also compatible with the results obtained by Harada *et al.* if they are normalized to the thermal cross section of JEFF-3.2. Our results are also compatible with most of the direct measurements of the resonance integral  $I_0$ , unlike other time-of-flight results.

Between 100 eV and 1 keV the disagreement with other experimental data and evaluations gradually decreases, in general, with the neutron energy. Above 1 keV our results are in reasonable agreement with most of the other experimental data and evaluations.

## ACKNOWLEDGMENTS

This work was supported in part by the Spanish national company for radioactive waste management ENRESA, through the CIEMAT-ENRESA agreements on “Transmutación de radionucleidos de vida larga como soporte a la gestión de residuos radioactivos de alta actividad,” the Spanish Plan Nacional de I+D+i de Física de Partículas (Projects No. FPA2016-76765-P and No. FPA2014-53290-C2-1-P) and the European Commission Seventh Framework Programme projects ANDES (No. FP7-249671) and CHANDA (No. FP7-605203).

## APPENDIX: RESONANCE PARAMETERS

The values of the resonance parameters obtained in this work are presented in Tables VI and VII, together with their corresponding uncertainties.  $\Gamma_{\gamma}$  values with uncertainties due to counting statistics larger than 10% were fixed to the average radiative capture width  $\langle \Gamma_{\gamma,0} \rangle = 45.4$  meV.

TABLE VI. Resonance parameters below 52 eV, together with their uncertainties due to counting statistics ( $\sigma_{\text{stat}}$ ), their total uncertainties due to systematic effects ( $\sigma_{\text{sys}}$ ) in the case of the  $\Gamma_\gamma$  parameters, and the sum of the uncertainties due to systematic effects with the exception of the 2.7% due to the normalization ( $\sigma_{\text{sys}^*}$ ) in the case of the  $g\Gamma_n$  parameters. Those  $\Gamma_\gamma$  that appear without uncertainties have been fixed to  $\langle\Gamma_{\gamma,0}\rangle = 45.4$  meV.

$E_0$ (eV)	$g\Gamma_n \pm \sigma_{\text{stat}} \pm \sigma_{\text{sys}^*}$ (meV)	$\Gamma_\gamma \pm \sigma_{\text{stat}} \pm \sigma_{\text{sys}}$ (meV)
0.3069	$0.03433 \pm 0.00004 \pm 0.00039$	$42.35 \pm 0.08 \pm 0.27$
0.5753	$0.06090 \pm 0.00008 \pm 0.00044$	$42.44 \pm 0.09 \pm 0.10$
1.2721	$0.21028 \pm 0.00012 \pm 0.00258$	$42.51 \pm 0.05 \pm 0.07$
1.9209	$0.07156 \pm 0.00010 \pm 0.00056$	$43.96 \pm 0.14 \pm 0.17$
2.3632	$0.04459 \pm 0.00012 \pm 0.00061$	$44.1 \pm 0.3 \pm 0.3$
2.5871	$0.09252 \pm 0.00016 \pm 0.00126$	$46.33 \pm 0.19 \pm 0.41$
3.9670	$0.1283 \pm 0.0003 \pm 0.0016$	$45.39 \pm 0.24 \pm 0.43$
4.9607	$0.1049 \pm 0.0003 \pm 0.0011$	$43.4 \pm 0.4 \pm 0.9$
5.4061	$0.4608 \pm 0.0007 \pm 0.0046$	$45.91 \pm 0.18 \pm 0.42$
6.1074	$0.0799 \pm 0.0004 \pm 0.0008$	$52.3 \pm 0.7 \pm 0.6$
6.7308	$0.0201 \pm 0.0003 \pm 0.0006$	$65.2 \pm 2.3 \pm 1.9$
7.6057	$0.00885 \pm 0.00034 \pm 0.00015$	45.4
7.6776	$0.0188 \pm 0.0005 \pm 0.0006$	$74 \pm 4 \pm 4$
8.1609	$0.0679 \pm 0.0005 \pm 0.0007$	$47.0 \pm 1.0 \pm 1.3$
9.0985	$0.2353 \pm 0.0008 \pm 0.0028$	$44.6 \pm 0.5 \pm 0.8$
9.8357	$0.2511 \pm 0.0009 \pm 0.0020$	$46.6 \pm 0.6 \pm 0.8$
10.103	$0.0170 \pm 0.0004 \pm 0.0005$	45.4
10.386	$0.2011 \pm 0.0009 \pm 0.0023$	$46.8 \pm 0.8 \pm 1.4$
10.979	$0.2562 \pm 0.0011 \pm 0.0021$	$51.4 \pm 0.7 \pm 1.6$
11.577	$0.0132 \pm 0.0004 \pm 0.0008$	45.4
11.875	$0.0046 \pm 0.0003 \pm 0.0007$	45.4
12.103	$0.0065 \pm 0.0003 \pm 0.0005$	45.4
12.859	$0.0801 \pm 0.0008 \pm 0.0022$	$45.7 \pm 1.8 \pm 2.9$
13.839	$0.0061 \pm 0.0004 \pm 0.0005$	45.4
14.339	$0.0418 \pm 0.0008 \pm 0.0003$	45.4
14.659	$1.466 \pm 0.003 \pm 0.014$	$45.5 \pm 0.4 \pm 1.0$
15.665	$0.1553 \pm 0.0013 \pm 0.0009$	$52.3 \pm 1.7 \pm 0.8$
16.362	$0.789 \pm 0.003 \pm 0.007$	$47.8 \pm 0.6 \pm 1.1$
16.823	$0.3980 \pm 0.0020 \pm 0.0052$	$46.0 \pm 1.0 \pm 1.5$
17.699	$0.2656 \pm 0.0017 \pm 0.0029$	$52.7 \pm 1.3 \pm 1.8$
18.137	$0.0144 \pm 0.0007 \pm 0.0004$	45.4
19.415	$0.1386 \pm 0.0015 \pm 0.0025$	$56.3 \pm 2.4 \pm 5.2$
20.287	$0.0193 \pm 0.0008 \pm 0.0008$	45.4
20.847	$0.0545 \pm 0.0010 \pm 0.0008$	45.4
21.719	$0.0528 \pm 0.0011 \pm 0.0009$	45.4
22.284	$0.0074 \pm 0.0007 \pm 0.0009$	45.4
22.714	$0.0503 \pm 0.0013 \pm 0.0009$	45.4
23.039	$0.2549 \pm 0.0033 \pm 0.0021$	$47.6 \pm 3.2 \pm 2.3$
23.297	$0.285 \pm 0.003 \pm 0.005$	$50 \pm 3 \pm 3$
24.151	$0.809 \pm 0.004 \pm 0.007$	$47.9 \pm 1.0 \pm 2.0$
25.592	$0.778 \pm 0.004 \pm 0.005$	$46.6 \pm 1.1 \pm 1.9$
26.459	$0.344 \pm 0.004 \pm 0.005$	$56 \pm 3 \pm 4$
26.637	$0.114 \pm 0.003 \pm 0.004$	45.4
27.538	$0.1297 \pm 0.0033 \pm 0.0022$	45.4
27.689	$0.275 \pm 0.005 \pm 0.009$	$51 \pm 4 \pm 5$
28.306	$0.371 \pm 0.004 \pm 0.005$	$45.5 \pm 2.5 \pm 1.4$
28.852	$0.292 \pm 0.003 \pm 0.005$	$50.6 \pm 3.1 \pm 2.5$
29.456	$0.4405 \pm 0.0038 \pm 0.0022$	$46.3 \pm 2.3 \pm 1.9$
29.889	$0.0352 \pm 0.0017 \pm 0.0015$	45.4
30.782	$0.1044 \pm 0.0027 \pm 0.0012$	45.4

TABLE VI. (*Continued.*)

$E_0$ (eV)	$g\Gamma_n \pm \sigma_{\text{stat}} \pm \sigma_{\text{sys}^*}$ (meV)	$\Gamma_\gamma \pm \sigma_{\text{stat}} \pm \sigma_{\text{sys}}$ (meV)
30.978	$0.2076 \pm 0.0042 \pm 0.0022$	45.4
31.199	$0.629 \pm 0.005 \pm 0.011$	$45.4 \pm 2.3 \pm 3.1$
31.978	$0.205 \pm 0.003 \pm 0.005$	$61 \pm 4 \pm 7$
33.508	$0.0332 \pm 0.0019 \pm 0.0012$	45.4
33.970	$0.379 \pm 0.004 \pm 0.004$	$41 \pm 3 \pm 3$
34.381	$0.0752 \pm 0.0024 \pm 0.0023$	45.4
34.869	$0.398 \pm 0.004 \pm 0.006$	$56 \pm 3 \pm 3$
35.426	$0.265 \pm 0.003 \pm 0.003$	45.4
36.227	$0.1152 \pm 0.0028 \pm 0.0013$	45.4
36.453	$0.0595 \pm 0.0029 \pm 0.0012$	45.4
36.917	$2.070 \pm 0.010 \pm 0.019$	$43.4 \pm 1.1 \pm 1.4$
37.823	$0.0040 \pm 0.0010 \pm 0.0003$	45.4
38.302	$1.441 \pm 0.009 \pm 0.007$	$43.4 \pm 1.6 \pm 1.3$
38.705	$0.0267 \pm 0.0025 \pm 0.0022$	45.4
39.553	$0.813 \pm 0.007 \pm 0.010$	$47.8 \pm 2.4 \pm 1.7$
40.003	$0.306 \pm 0.005 \pm 0.006$	45.4
40.330	$0.604 \pm 0.007 \pm 0.011$	$64 \pm 4 \pm 3$
41.242	$0.0603 \pm 0.0027 \pm 0.0021$	45.4
41.717	$0.254 \pm 0.004 \pm 0.003$	45.4
42.074	$0.122 \pm 0.003 \pm 0.003$	45.4
43.226	$0.589 \pm 0.006 \pm 0.005$	45.4
43.512	$0.386 \pm 0.005 \pm 0.003$	45.4
44.329	$0.117 \pm 0.003 \pm 0.003$	45.4
44.594	$0.076 \pm 0.004 \pm 0.007$	45.4
44.852	$0.092 \pm 0.003 \pm 0.006$	45.4
45.993	$0.4398 \pm 0.0055 \pm 0.0018$	45.4
46.489	$0.271 \pm 0.005 \pm 0.004$	45.4
47.454	$0.682 \pm 0.007 \pm 0.010$	$39 \pm 3 \pm 3$
48.685	$0.460 \pm 0.006 \pm 0.006$	45.4
49.239	$0.126 \pm 0.004 \pm 0.004$	45.4
50.065	$0.0149 \pm 0.0045 \pm 0.0015$	45.4
50.195	$1.529 \pm 0.014 \pm 0.014$	$35.1 \pm 2.5 \pm 2.9$
50.763	$0.259 \pm 0.005 \pm 0.006$	45.4
51.896	$0.827 \pm 0.008 \pm 0.018$	$36 \pm 3 \pm 5$

TABLE VII. Resonance energies and  $g\Gamma_n$  parameters between 52 and 700 eV together with the uncertainties due to counting statistics ( $\sigma_{\text{stat}}$ ) and the sum of the uncertainties due to systematic effects with the exception of the 2.7% due to the normalization ( $\sigma_{\text{sys}^*}$ ). The value of  $\Gamma_\gamma$  is not shown, as it corresponds to  $\langle\Gamma_{\gamma,0}\rangle = 45.4$  meV for all resonances.

$E_0$ (eV)	$g\Gamma_n$ (meV)	$\pm$	$\sigma_{\text{stat}}$ (meV)	$\pm$	$\sigma_{\text{sys}^*}$ (meV)
52.907	0.0964	$\pm$	0.0038	$\pm$	0.0022
53.403	0.108	$\pm$	0.004	$\pm$	0.006
54.312	0.054	$\pm$	0.004	$\pm$	0.003
54.760	0.137	$\pm$	0.008	$\pm$	0.007
54.922	0.653	$\pm$	0.010	$\pm$	0.009
55.505	0.127	$\pm$	0.005	$\pm$	0.003
55.862	0.889	$\pm$	0.012	$\pm$	0.017
56.077	0.5265	$\pm$	0.0099	$\pm$	0.0024





TABLE VII. (*Continued.*)

$E_0$ (eV)	$g\Gamma_n$ (meV)	$\pm$	$\sigma_{\text{stat}}$ (meV)	$\pm$	$\sigma_{\text{sys}^*}$ (meV)
140.900	1.03	$\pm$	0.04	$\pm$	0.03
141.226	4.25	$\pm$	0.08	$\pm$	0.07
142.924	0.409	$\pm$	0.020	$\pm$	0.021
144.617	1.00	$\pm$	0.03	$\pm$	0.04
145.111	0.329	$\pm$	0.021	$\pm$	0.019
146.212	1.26	$\pm$	0.03	$\pm$	0.04
147.770	7.00	$\pm$	0.11	$\pm$	0.07
148.082	1.06	$\pm$	0.05	$\pm$	0.04
148.908	2.53	$\pm$	0.05	$\pm$	0.03
150.933	0.325	$\pm$	0.022	$\pm$	0.022
151.587	1.176	$\pm$	0.032	$\pm$	0.025
152.864	1.28	$\pm$	0.04	$\pm$	0.04
153.338	0.264	$\pm$	0.022	$\pm$	0.009
155.036	0.548	$\pm$	0.082	$\pm$	0.022
155.133	1.13	$\pm$	0.10	$\pm$	0.04
155.625	0.406	$\pm$	0.029	$\pm$	0.022
156.305	2.73	$\pm$	0.05	$\pm$	0.09
157.007	0.975	$\pm$	0.118	$\pm$	0.010
158.140	0.871	$\pm$	0.031	$\pm$	0.023
159.194	3.44	$\pm$	0.06	$\pm$	0.04
159.809	0.739	$\pm$	0.031	$\pm$	0.015
161.847	1.64	$\pm$	0.06	$\pm$	0.05
162.134	1.55	$\pm$	0.06	$\pm$	0.03
163.329	5.51	$\pm$	0.08	$\pm$	0.09
164.982	4.60	$\pm$	0.09	$\pm$	0.04
165.354	0.96	$\pm$	0.05	$\pm$	0.04
166.326	0.210	$\pm$	0.021	$\pm$	0.024
167.276	2.12	$\pm$	0.05	$\pm$	0.03
167.732	0.627	$\pm$	0.034	$\pm$	0.023
168.437	0.23	$\pm$	0.02	$\pm$	0.04
170.585	1.02	$\pm$	0.03	$\pm$	0.04
171.212	0.35	$\pm$	0.03	$\pm$	0.03
171.778	0.094	$\pm$	0.017	$\pm$	0.024
172.776	0.189	$\pm$	0.020	$\pm$	0.014
173.946	1.81	$\pm$	0.05	$\pm$	0.05
174.402	0.53	$\pm$	0.03	$\pm$	0.03
175.288	0.386	$\pm$	0.026	$\pm$	0.022
176.039	0.90	$\pm$	0.03	$\pm$	0.03
177.020	0.575	$\pm$	0.034	$\pm$	0.008
177.465	0.62	$\pm$	0.03	$\pm$	0.03
178.285	1.01	$\pm$	0.04	$\pm$	0.04
179.149	1.189	$\pm$	0.038	$\pm$	0.024
180.222	1.71	$\pm$	0.05	$\pm$	0.04
180.854	0.39	$\pm$	0.03	$\pm$	0.04
181.636	0.68	$\pm$	0.04	$\pm$	0.03
181.955	0.60	$\pm$	0.04	$\pm$	0.04
182.876	3.11	$\pm$	0.06	$\pm$	0.10
183.652	0.32	$\pm$	0.03	$\pm$	0.03
184.780	4.86	$\pm$	0.09	$\pm$	0.10
186.057	2.62	$\pm$	0.06	$\pm$	0.08
187.190	0.644	$\pm$	0.033	$\pm$	0.020
187.923	0.338	$\pm$	0.035	$\pm$	0.016
188.305	0.52	$\pm$	0.04	$\pm$	0.03
188.947	0.77	$\pm$	0.04	$\pm$	0.03
189.752	0.652	$\pm$	0.032	$\pm$	0.023
190.859	0.96	$\pm$	0.04	$\pm$	0.05

TABLE VII. (*Continued.*)

$E_0$ (eV)	$g\Gamma_n$ (meV)	$\pm$	$\sigma_{\text{stat}}$ (meV)	$\pm$	$\sigma_{\text{sys}^*}$ (meV)
191.756	0.817	$\pm$	0.040	$\pm$	0.014
192.410	4.11	$\pm$	0.08	$\pm$	0.08
193.334	4.58	$\pm$	0.10	$\pm$	0.06
194.001	0.26	$\pm$	0.03	$\pm$	0.04
194.993	0.251	$\pm$	0.024	$\pm$	0.020
197.053	4.33	$\pm$	0.08	$\pm$	0.03
198.200	0.77	$\pm$	0.04	$\pm$	0.03
198.821	0.515	$\pm$	0.033	$\pm$	0.016
199.889	0.30	$\pm$	0.03	$\pm$	0.04
200.649	1.92	$\pm$	0.06	$\pm$	0.04
200.994	0.236	$\pm$	0.038	$\pm$	0.015
201.696	0.666	$\pm$	0.039	$\pm$	0.020
202.392	2.78	$\pm$	0.07	$\pm$	0.07
203.094	0.27	$\pm$	0.03	$\pm$	0.04
203.844	0.87	$\pm$	0.04	$\pm$	0.04
204.836	2.91	$\pm$	0.10	$\pm$	0.03
205.218	5.52	$\pm$	0.13	$\pm$	0.13
207.864	0.56	$\pm$	0.04	$\pm$	0.03
208.680	0.90	$\pm$	0.05	$\pm$	0.04
209.417	6.07	$\pm$	0.14	$\pm$	0.18
210.068	1.25	$\pm$	0.05	$\pm$	0.03
211.731	3.67	$\pm$	0.08	$\pm$	0.09
212.987	1.89	$\pm$	0.07	$\pm$	0.07
213.513	1.860	$\pm$	0.064	$\pm$	0.019
214.689	4.10	$\pm$	0.09	$\pm$	0.05
217.100	0.31	$\pm$	0.03	$\pm$	0.03
217.872	1.84	$\pm$	0.06	$\pm$	0.03
219.375	2.67	$\pm$	0.07	$\pm$	0.06
220.028	1.813	$\pm$	0.062	$\pm$	0.017
222.587	0.43	$\pm$	0.04	$\pm$	0.03
223.180	1.07	$\pm$	0.05	$\pm$	0.05
224.082	3.71	$\pm$	0.10	$\pm$	0.04
224.891	2.484	$\pm$	0.071	$\pm$	0.023
225.891	0.25	$\pm$	0.03	$\pm$	0.04
227.542	2.920	$\pm$	0.080	$\pm$	0.025
228.135	0.82	$\pm$	0.05	$\pm$	0.04
230.929	0.45	$\pm$	0.04	$\pm$	0.04
233.526	6.72	$\pm$	0.14	$\pm$	0.06
234.438	1.88	$\pm$	0.07	$\pm$	0.07
236.932	1.98	$\pm$	0.06	$\pm$	0.05
238.904	1.70	$\pm$	0.06	$\pm$	0.03
240.257	0.77	$\pm$	0.05	$\pm$	0.03
241.438	2.44	$\pm$	0.08	$\pm$	0.03
242.749	2.06	$\pm$	0.08	$\pm$	0.05
243.185	1.14	$\pm$	0.07	$\pm$	0.11
244.066	0.685	$\pm$	0.045	$\pm$	0.020
246.226	0.97	$\pm$	0.05	$\pm$	0.04
247.136	2.28	$\pm$	0.07	$\pm$	0.07
249.529	0.517	$\pm$	0.045	$\pm$	0.019
250.640	2.40	$\pm$	0.09	$\pm$	0.10
251.224	2.86	$\pm$	0.16	$\pm$	0.07
251.559	2.95	$\pm$	0.13	$\pm$	0.04
252.715	1.62	$\pm$	0.09	$\pm$	0.05
253.130	2.61	$\pm$	0.12	$\pm$	0.17
253.749	1.37	$\pm$	0.07	$\pm$	0.04
255.584	1.00	$\pm$	0.05	$\pm$	0.05

TABLE VII. (Continued.)

$E_0$ (eV)	$g\Gamma_n$ (meV)	$\pm$	$\sigma_{\text{stat}}$ (meV)	$\pm$	$\sigma_{\text{sys}*}$ (meV)
256.810	0.56	$\pm$	0.05	$\pm$	0.04
257.709	0.40	$\pm$	0.04	$\pm$	0.04
259.770	6.33	$\pm$	0.15	$\pm$	0.06
260.804	1.79	$\pm$	0.08	$\pm$	0.06
261.927	2.21	$\pm$	0.08	$\pm$	0.07
263.043	0.84	$\pm$	0.06	$\pm$	0.03
264.019	1.31	$\pm$	0.07	$\pm$	0.03
264.751	2.13	$\pm$	0.08	$\pm$	0.06
266.078	0.66	$\pm$	0.05	$\pm$	0.04
267.467	1.59	$\pm$	0.07	$\pm$	0.06
268.644	2.12	$\pm$	0.08	$\pm$	0.07
269.770	3.20	$\pm$	0.12	$\pm$	0.07
270.422	4.68	$\pm$	0.15	$\pm$	0.06
271.801	0.87	$\pm$	0.06	$\pm$	0.04
272.836	1.28	$\pm$	0.07	$\pm$	0.03
274.660	6.63	$\pm$	0.27	$\pm$	0.20
274.991	3.47	$\pm$	0.19	$\pm$	0.08
275.825	1.091	$\pm$	0.066	$\pm$	0.022
276.891	0.52	$\pm$	0.05	$\pm$	0.03
277.622	0.520	$\pm$	0.052	$\pm$	0.022
278.444	0.35	$\pm$	0.04	$\pm$	0.04
279.683	0.45	$\pm$	0.05	$\pm$	0.03
281.087	3.54	$\pm$	0.14	$\pm$	0.06
281.496	1.85	$\pm$	0.13	$\pm$	0.05
282.152	0.95	$\pm$	0.10	$\pm$	0.13
282.624	1.77	$\pm$	0.12	$\pm$	0.04
283.427	14.3	$\pm$	0.4	$\pm$	0.4
284.777	1.79	$\pm$	0.08	$\pm$	0.05
286.125	2.38	$\pm$	0.11	$\pm$	0.10
286.635	3.35	$\pm$	0.15	$\pm$	0.07
287.512	1.36	$\pm$	0.08	$\pm$	0.04
288.824	2.29	$\pm$	0.10	$\pm$	0.05
289.557	4.39	$\pm$	0.19	$\pm$	0.09
290.043	2.89	$\pm$	0.13	$\pm$	0.09
291.167	0.98	$\pm$	0.07	$\pm$	0.08
292.604	2.24	$\pm$	0.10	$\pm$	0.07
293.502	1.08	$\pm$	0.07	$\pm$	0.08
294.957	2.16	$\pm$	0.09	$\pm$	0.05
296.389	3.692	$\pm$	0.129	$\pm$	0.022
297.113	3.85	$\pm$	0.14	$\pm$	0.03
297.828	0.47	$\pm$	0.06	$\pm$	0.04
298.738	2.95	$\pm$	0.12	$\pm$	0.08
299.794	7.44	$\pm$	0.20	$\pm$	0.08
300.692	3.07	$\pm$	0.12	$\pm$	0.07
302.205	4.99	$\pm$	0.14	$\pm$	0.06
303.832	1.36	$\pm$	0.08	$\pm$	0.03
304.581	1.21	$\pm$	0.08	$\pm$	0.04
305.831	0.85	$\pm$	0.06	$\pm$	0.04
307.162	3.09	$\pm$	0.11	$\pm$	0.07
307.996	0.69	$\pm$	0.07	$\pm$	0.04
309.017	3.34	$\pm$	0.16	$\pm$	0.06
309.435	1.78	$\pm$	0.13	$\pm$	0.03
310.297	2.16	$\pm$	0.10	$\pm$	0.03
311.782	2.27	$\pm$	0.10	$\pm$	0.04
313.515	1.96	$\pm$	0.10	$\pm$	0.07
314.334	2.96	$\pm$	0.12	$\pm$	0.10

TABLE VII. (Continued.)

$E_0$ (eV)	$g\Gamma_n$ (meV)	$\pm$	$\sigma_{\text{stat}}$ (meV)	$\pm$	$\sigma_{\text{sys}*}$ (meV)
316.734	3.51	$\pm$	0.14	$\pm$	0.08
317.480	2.45	$\pm$	0.14	$\pm$	0.13
318.143	1.41	$\pm$	0.10	$\pm$	0.07
320.480	3.03	$\pm$	0.12	$\pm$	0.04
321.888	1.62	$\pm$	0.10	$\pm$	0.10
322.911	1.33	$\pm$	0.09	$\pm$	0.06
324.375	5.88	$\pm$	0.22	$\pm$	0.19
325.565	3.51	$\pm$	0.14	$\pm$	0.14
326.670	1.37	$\pm$	0.10	$\pm$	0.09
327.790	0.98	$\pm$	0.08	$\pm$	0.03
331.615	0.75	$\pm$	0.09	$\pm$	0.05
332.411	1.72	$\pm$	0.12	$\pm$	0.13
333.215	1.18	$\pm$	0.11	$\pm$	0.12
334.461	5.7	$\pm$	0.3	$\pm$	0.3
335.318	2.03	$\pm$	0.15	$\pm$	0.12
335.928	1.49	$\pm$	0.13	$\pm$	0.04
338.935	2.95	$\pm$	0.16	$\pm$	0.09
339.791	1.77	$\pm$	0.12	$\pm$	0.21
341.228	4.13	$\pm$	0.18	$\pm$	0.17
342.307	1.95	$\pm$	0.13	$\pm$	0.14
343.636	1.42	$\pm$	0.13	$\pm$	0.11
344.393	5.22	$\pm$	0.27	$\pm$	0.18
345.304	7.60	$\pm$	0.30	$\pm$	0.16
346.030	1.26	$\pm$	0.16	$\pm$	0.05
346.506	0.75	$\pm$	0.13	$\pm$	0.06
347.324	7.10	$\pm$	0.29	$\pm$	0.13
349.619	2.09	$\pm$	0.13	$\pm$	0.07
350.786	3.20	$\pm$	0.15	$\pm$	0.06
351.796	1.17	$\pm$	0.11	$\pm$	0.09
353.017	2.62	$\pm$	0.17	$\pm$	0.06
353.570	3.32	$\pm$	0.21	$\pm$	0.19
354.463	0.85	$\pm$	0.10	$\pm$	0.09
355.478	1.00	$\pm$	0.10	$\pm$	0.08
356.455	0.84	$\pm$	0.09	$\pm$	0.04
357.618	3.37	$\pm$	0.15	$\pm$	0.05
359.245	6.16	$\pm$	0.23	$\pm$	0.12
360.333	3.32	$\pm$	0.16	$\pm$	0.13
361.707	8.3	$\pm$	0.4	$\pm$	0.3
362.392	4.65	$\pm$	0.27	$\pm$	0.19
363.371	7.90	$\pm$	0.31	$\pm$	0.24
364.366	26.7	$\pm$	1.3	$\pm$	1.4
366.635	0.98	$\pm$	0.09	$\pm$	0.09
368.154	0.59	$\pm$	0.08	$\pm$	0.07
369.525	0.85	$\pm$	0.09	$\pm$	0.05
370.540	3.5	$\pm$	0.2	$\pm$	0.3
373.233	5.06	$\pm$	0.23	$\pm$	0.13
373.770	1.47	$\pm$	0.14	$\pm$	0.13
375.380	4.06	$\pm$	0.17	$\pm$	0.12
376.492	1.44	$\pm$	0.13	$\pm$	0.08
377.201	1.67	$\pm$	0.13	$\pm$	0.06
378.874	2.05	$\pm$	0.13	$\pm$	0.04
380.894	3.97	$\pm$	0.17	$\pm$	0.18
382.094	2.17	$\pm$	0.14	$\pm$	0.09
384.583	5.18	$\pm$	0.25	$\pm$	0.08
385.346	2.58	$\pm$	0.18	$\pm$	0.11
386.159	3.04	$\pm$	0.21	$\pm$	0.19

TABLE VII. (Continued.)

$E_0$ (eV)	$g\Gamma_n$ (meV)	$\pm$	$\sigma_{\text{stat}}$ (meV)	$\pm$	$\sigma_{\text{sys}*}$ (meV)
386.895	6.80	$\pm$	0.28	$\pm$	0.15
387.830	3.22	$\pm$	0.16	$\pm$	0.16
390.607	2.40	$\pm$	0.15	$\pm$	0.04
391.891	3.3	$\pm$	0.2	$\pm$	0.3
393.776	1.85	$\pm$	0.14	$\pm$	0.09
394.658	3.26	$\pm$	0.17	$\pm$	0.07
395.744	1.13	$\pm$	0.13	$\pm$	0.06
396.430	6.11	$\pm$	0.30	$\pm$	0.22
397.600	3.92	$\pm$	0.20	$\pm$	0.09
398.674	2.08	$\pm$	0.14	$\pm$	0.05
399.960	7.70	$\pm$	0.28	$\pm$	0.22
401.820	5.90	$\pm$	0.23	$\pm$	0.19
402.848	0.42	$\pm$	0.08	$\pm$	0.05
404.031	1.48	$\pm$	0.12	$\pm$	0.16
405.147	1.36	$\pm$	0.12	$\pm$	0.07
406.150	0.96	$\pm$	0.11	$\pm$	0.09
407.114	2.38	$\pm$	0.15	$\pm$	0.11
408.196	1.89	$\pm$	0.16	$\pm$	0.07
408.740	1.80	$\pm$	0.16	$\pm$	0.19
410.499	0.88	$\pm$	0.10	$\pm$	0.03
411.916	0.61	$\pm$	0.08	$\pm$	0.10
413.379	1.23	$\pm$	0.12	$\pm$	0.03
414.133	1.30	$\pm$	0.13	$\pm$	0.04
415.045	1.59	$\pm$	0.13	$\pm$	0.06
416.520	2.53	$\pm$	0.16	$\pm$	0.14
417.401	3.26	$\pm$	0.20	$\pm$	0.16
418.461	2.59	$\pm$	0.16	$\pm$	0.14
420.736	3.55	$\pm$	0.20	$\pm$	0.10
421.492	3.63	$\pm$	0.21	$\pm$	0.12
422.557	1.60	$\pm$	0.13	$\pm$	0.11
424.394	3.55	$\pm$	0.20	$\pm$	0.08
425.530	3.83	$\pm$	0.20	$\pm$	0.15
426.576	3.24	$\pm$	0.19	$\pm$	0.17
427.435	1.22	$\pm$	0.14	$\pm$	0.10
428.397	5.1	$\pm$	0.3	$\pm$	0.3
429.110	1.14	$\pm$	0.14	$\pm$	0.08
430.104	2.50	$\pm$	0.16	$\pm$	0.11
431.257	3.96	$\pm$	0.20	$\pm$	0.14
433.440	5.68	$\pm$	0.32	$\pm$	0.17
434.155	5.28	$\pm$	0.27	$\pm$	0.09
435.342	0.730	$\pm$	0.104	$\pm$	0.023
436.307	2.00	$\pm$	0.16	$\pm$	0.12
437.268	0.24	$\pm$	0.06	$\pm$	0.03
438.289	1.07	$\pm$	0.12	$\pm$	0.07
439.190	1.33	$\pm$	0.15	$\pm$	0.10
440.037	4.37	$\pm$	0.32	$\pm$	0.23
440.706	8.53	$\pm$	0.40	$\pm$	0.23
441.959	1.82	$\pm$	0.15	$\pm$	0.03
443.090	2.56	$\pm$	0.17	$\pm$	0.08
444.791	9.56	$\pm$	0.44	$\pm$	0.12
446.497	8.48	$\pm$	0.36	$\pm$	0.16
447.369	3.28	$\pm$	0.20	$\pm$	0.13
449.100	0.362	$\pm$	0.105	$\pm$	0.010
449.371	2.91	$\pm$	0.21	$\pm$	0.06
450.493	1.03	$\pm$	0.13	$\pm$	0.09
451.659	2.06	$\pm$	0.31	$\pm$	0.09

TABLE VII. (Continued.)

$E_0$ (eV)	$g\Gamma_n$ (meV)	$\pm$	$\sigma_{\text{stat}}$ (meV)	$\pm$	$\sigma_{\text{sys}*}$ (meV)
451.932	2.78	$\pm$	0.35	$\pm$	0.07
453.112	17.9	$\pm$	0.9	$\pm$	0.7
454.607	4.2	$\pm$	0.2	$\pm$	0.3
456.905	2.21	$\pm$	0.19	$\pm$	0.11
457.735	8.64	$\pm$	0.44	$\pm$	0.24
458.529	6.28	$\pm$	0.32	$\pm$	0.14
460.092	2.5	$\pm$	0.2	$\pm$	0.3
461.227	2.48	$\pm$	0.18	$\pm$	0.20
462.924	2.46	$\pm$	0.20	$\pm$	0.11
463.765	2.05	$\pm$	0.20	$\pm$	0.13
464.611	3.8	$\pm$	0.2	$\pm$	0.4
466.045	9.9	$\pm$	0.5	$\pm$	0.6
466.979	5.43	$\pm$	0.39	$\pm$	0.20
467.743	7.8	$\pm$	0.4	$\pm$	0.3
469.044	3.29	$\pm$	0.21	$\pm$	0.05
471.752	2.14	$\pm$	0.16	$\pm$	0.18
472.975	2.76	$\pm$	0.20	$\pm$	0.19
474.037	1.37	$\pm$	0.16	$\pm$	0.09
475.064	9.4	$\pm$	0.5	$\pm$	0.4
476.170	2.2	$\pm$	0.2	$\pm$	0.3
479.858	11.7	$\pm$	0.5	$\pm$	0.7
481.165	6.44	$\pm$	0.39	$\pm$	0.06
481.910	2.01	$\pm$	0.19	$\pm$	0.19
483.764	6.83	$\pm$	0.32	$\pm$	0.10
484.965	5.8	$\pm$	0.3	$\pm$	0.3
486.259	3.17	$\pm$	0.24	$\pm$	0.25
487.008	3.92	$\pm$	0.29	$\pm$	0.17
488.159	4.4	$\pm$	0.2	$\pm$	0.4
489.906	2.82	$\pm$	0.22	$\pm$	0.22
490.787	2.04	$\pm$	0.23	$\pm$	0.16
491.767	15.5	$\pm$	0.7	$\pm$	0.6
493.472	2.08	$\pm$	0.17	$\pm$	0.17
494.968	1.21	$\pm$	0.15	$\pm$	0.07
495.758	1.08	$\pm$	0.15	$\pm$	0.14
496.723	2.51	$\pm$	0.20	$\pm$	0.22
498.708	1.90	$\pm$	0.19	$\pm$	0.19
499.499	6.19	$\pm$	0.32	$\pm$	0.08
502.333	1.48	$\pm$	0.16	$\pm$	0.10
503.540	6.19	$\pm$	0.38	$\pm$	0.16
504.243	6.0	$\pm$	0.4	$\pm$	0.3
505.747	1.13	$\pm$	0.15	$\pm$	0.17
506.853	1.63	$\pm$	0.17	$\pm$	0.10
508.072	1.49	$\pm$	0.16	$\pm$	0.09
509.519	1.87	$\pm$	0.18	$\pm$	0.09
510.964	3.1	$\pm$	0.2	$\pm$	0.3
512.842	3.40	$\pm$	0.22	$\pm$	0.20
515.115	1.54	$\pm$	0.17	$\pm$	0.18
516.675	5.5	$\pm$	0.3	$\pm$	0.4
518.719	12.7	$\pm$	0.7	$\pm$	0.7
521.371	4.45	$\pm$	0.27	$\pm$	0.10
522.472	2.60	$\pm$	0.21	$\pm$	0.18
525.323	3.62	$\pm$	0.26	$\pm$	0.06
526.327	1.18	$\pm$	0.16	$\pm$	0.11
527.682	0.66	$\pm$	0.13	$\pm$	0.06
528.996	11.4	$\pm$	0.6	$\pm$	0.5
529.606	2.56	$\pm$	0.31	$\pm$	0.20

TABLE VII. (Continued.)

TABLE VII. (Continued.)

$E_0$ (eV)	$g\Gamma_n$ (meV)	$\pm$	$\sigma_{stat}$ (meV)	$\pm$	$\sigma_{sys*}$ (meV)
531.226	3.44	$\pm$	0.28	$\pm$	0.15
532.274	7.8	$\pm$	0.4	$\pm$	0.6
533.788	1.93	$\pm$	0.23	$\pm$	0.14
534.643	5.52	$\pm$	0.34	$\pm$	0.18
536.013	2.34	$\pm$	0.25	$\pm$	0.11
536.821	5.4	$\pm$	0.4	$\pm$	0.4
538.434	1.67	$\pm$	0.18	$\pm$	0.13
540.165	7.5	$\pm$	0.5	$\pm$	0.4
541.190	1.55	$\pm$	0.18	$\pm$	0.22
543.256	6.43	$\pm$	0.40	$\pm$	0.17
544.542	4.4	$\pm$	0.3	$\pm$	0.4
545.558	5.84	$\pm$	0.39	$\pm$	0.18
546.927	0.88	$\pm$	0.14	$\pm$	0.11
549.036	5.27	$\pm$	0.30	$\pm$	0.11
550.529	2.22	$\pm$	0.25	$\pm$	0.17
551.250	4.97	$\pm$	0.38	$\pm$	0.17
552.821	1.28	$\pm$	0.19	$\pm$	0.11
553.667	6.0	$\pm$	0.4	$\pm$	0.4
555.315	3.89	$\pm$	0.25	$\pm$	0.18
558.830	1.49	$\pm$	0.20	$\pm$	0.07
559.566	1.84	$\pm$	0.21	$\pm$	0.05
561.643	1.71	$\pm$	0.19	$\pm$	0.06
563.198	8.7	$\pm$	0.5	$\pm$	0.3
564.066	3.77	$\pm$	0.32	$\pm$	0.12
565.256	2.8	$\pm$	0.2	$\pm$	0.3
567.094	1.47	$\pm$	0.18	$\pm$	0.11
568.177	1.50	$\pm$	0.20	$\pm$	0.09
569.134	1.61	$\pm$	0.19	$\pm$	0.17
571.937	3.7	$\pm$	0.3	$\pm$	0.3
574.460	5.0	$\pm$	0.3	$\pm$	0.3
575.804	3.90	$\pm$	0.33	$\pm$	0.08
576.977	7.5	$\pm$	0.4	$\pm$	0.3
578.793	8.2	$\pm$	0.4	$\pm$	0.4
580.696	3.8	$\pm$	0.3	$\pm$	0.3
583.049	9.1	$\pm$	0.5	$\pm$	0.6
584.216	3.00	$\pm$	0.30	$\pm$	0.17
585.133	2.0	$\pm$	0.2	$\pm$	0.3
587.201	0.67	$\pm$	0.14	$\pm$	0.14
588.620	4.46	$\pm$	0.37	$\pm$	0.23
589.601	17.4	$\pm$	1.4	$\pm$	1.2
590.382	3.2	$\pm$	0.4	$\pm$	0.3
593.140	33.0	$\pm$	1.8	$\pm$	1.0
595.391	0.7	$\pm$	0.2	$\pm$	0.3
596.873	5.6	$\pm$	0.5	$\pm$	0.4
597.585	3.38	$\pm$	0.33	$\pm$	0.17
599.457	1.61	$\pm$	0.20	$\pm$	0.20
601.391	1.38	$\pm$	0.19	$\pm$	0.12
602.810	6.2	$\pm$	0.5	$\pm$	0.3
603.599	5.2	$\pm$	0.5	$\pm$	0.4
605.075	1.57	$\pm$	0.20	$\pm$	0.11
606.565	4.2	$\pm$	0.3	$\pm$	0.3
607.930	25	$\pm$	2	$\pm$	3
608.692	8.4	$\pm$	0.7	$\pm$	0.3
609.804	1.37	$\pm$	0.21	$\pm$	0.06
610.753	0.99	$\pm$	0.17	$\pm$	0.08
612.676	10.2	$\pm$	0.8	$\pm$	0.6
613.457	12.9	$\pm$	0.8	$\pm$	0.7

$E_0$ (eV)	$g\Gamma_n$ (meV)	$\pm$	$\sigma_{stat}$ (meV)	$\pm$	$\sigma_{sys*}$ (meV)
616.795	1.13	$\pm$	0.18	$\pm$	0.19
618.323	3.09	$\pm$	0.26	$\pm$	0.15
619.953	2.24	$\pm$	0.27	$\pm$	0.07
620.827	3.12	$\pm$	0.30	$\pm$	0.21
622.134	1.61	$\pm$	0.21	$\pm$	0.19
623.382	3.35	$\pm$	0.34	$\pm$	0.12
624.374	5.80	$\pm$	0.41	$\pm$	0.09
625.892	2.35	$\pm$	0.25	$\pm$	0.25
627.802	5.3	$\pm$	0.4	$\pm$	0.4
629.956	7.1	$\pm$	0.6	$\pm$	0.3
630.898	9.4	$\pm$	0.7	$\pm$	0.5
632.961	4.14	$\pm$	0.33	$\pm$	0.18
634.265	5.39	$\pm$	0.46	$\pm$	0.11
635.347	7.06	$\pm$	0.54	$\pm$	0.12
636.918	1.18	$\pm$	0.20	$\pm$	0.21
637.658	1.286	$\pm$	0.212	$\pm$	0.024
639.711	10.02	$\pm$	0.62	$\pm$	0.23
640.761	6.1	$\pm$	0.5	$\pm$	0.4
641.739	1.46	$\pm$	0.23	$\pm$	0.17
642.944	1.87	$\pm$	0.26	$\pm$	0.19
644.250	6.32	$\pm$	0.46	$\pm$	0.14
645.351	3.4	$\pm$	0.4	$\pm$	0.3
646.301	3.54	$\pm$	0.33	$\pm$	0.23
648.282	5.2	$\pm$	0.4	$\pm$	0.3
650.678	9.7	$\pm$	0.6	$\pm$	0.9
652.221	11.7	$\pm$	0.8	$\pm$	0.3
654.070	3.84	$\pm$	0.32	$\pm$	0.12
656.381	6.0	$\pm$	0.5	$\pm$	0.8
658.355	11.4	$\pm$	0.8	$\pm$	0.4
659.214	6.1	$\pm$	0.5	$\pm$	1.1
661.683	4.7	$\pm$	0.4	$\pm$	0.6
662.858	3.7	$\pm$	0.3	$\pm$	0.3
664.996	3.44	$\pm$	0.34	$\pm$	0.25
666.407	4.44	$\pm$	0.41	$\pm$	0.10
667.346	3.2	$\pm$	0.4	$\pm$	0.3
668.280	2.94	$\pm$	0.33	$\pm$	0.18
670.056	7.7	$\pm$	0.7	$\pm$	0.8
670.758	11.2	$\pm$	1.5	$\pm$	0.7
671.184	1.68	$\pm$	0.44	$\pm$	0.14
672.487	13.3	$\pm$	0.9	$\pm$	0.5
673.671	5.5	$\pm$	0.5	$\pm$	0.6
675.929	5.1	$\pm$	0.4	$\pm$	0.3
677.163	8.6	$\pm$	0.7	$\pm$	0.7
678.539	4.8	$\pm$	0.4	$\pm$	0.4
679.916	5.0	$\pm$	0.4	$\pm$	0.4
682.073	3.0	$\pm$	0.3	$\pm$	0.3
683.339	1.06	$\pm$	0.19	$\pm$	0.08
685.235	12.7	$\pm$	1.0	$\pm$	0.5
685.970	11.8	$\pm$	0.9	$\pm$	1.3
687.541	1.12	$\pm$	0.21	$\pm$	0.06
688.732	5.64	$\pm$	0.49	$\pm$	0.13
690.399	8.3	$\pm$	0.6	$\pm$	0.3
692.310	5.9	$\pm$	0.5	$\pm$	0.3
694.320	3.45	$\pm$	0.32	$\pm$	0.15
696.943	6.4	$\pm$	0.5	$\pm$	0.4
699.189	4.0	$\pm$	0.4	$\pm$	0.3
700.419	5.28	$\pm$	0.46	$\pm$	0.21

- [1] G. Aliberti, G. Palmiotti, M. Salvatores, and C. G. Stenberg, *Nucl. Sci. Eng.* **146**, 13 (2004).
- [2] G. Aliberti, G. Palmiotti, M. Salvatores, T. K. Kim, T. A. Taiwo, M. Anitescu, I. Kodeli, E. Sartori, J. C. Bosq, and J. Tommasi, *Ann. Nucl. Energy* **33**, 700 (2006).
- [3] M. Salvatores *et al.*, Uncertainty and target accuracy assessment for innovative systems using recent covariance data evaluations, Technical Report No. 6410, NEA/WPEC-26, OECD, Paris, France, 2008.
- [4] K. Fraval *et al.* (n\_TOF Collaboration), *Phys. Rev. C* **89**, 044609 (2014).
- [5] C. Lampoudis, S. Kopecky, O. Bouland, F. Gunsing, G. Noguere, A. J. M. Plompen, C. Sage, P. Schillebeeckx, and R. Wynants, *Eur. Phys. J. Plus* **128**, 86 (2013).
- [6] G. Žerovnik, P. Schillebeeckx, D. Cano-Ott, M. Jandel, J. Hori, A. Kimura, M. Rossbach, A. Letourneau, G. Noguere, P. Leconte, T. Sano, M. A. Kellett, O. Iwamoto, A. V. Ignatyuk, O. Cabellos, C. Genreith, and H. Harada, *EPJ Web Conf.* **146**, 11035 (2017).
- [7] C. Guerrero *et al.* (n\_TOF Collaboration), *Eur. Phys. J. A* **49**, 27 (2013).
- [8] N. Otuka *et al.*, *Nucl. Data Sheets* **120**, 272 (2014).
- [9] U. Abbondanno *et al.* (n\_TOF Collaboration), CERN n\_TOF Facility: Performance Report, Technical Report No. INTC-2002-037, CERN, 2003.
- [10] E. Berthoumieux *et al.* (n\_TOF Collaboration), The neutron Time-of-Flight facility, n\_TOF, at CERN (I): Technical Description, Technical Report No. CERN-n\_TOF-PUB-2013-001, CERN, 2013.
- [11] C. Weiß *et al.* (n\_TOF Collaboration), *Nucl. Instrum. Methods A* **799**, 90 (2015).
- [12] M. Barbagallo *et al.* (n\_TOF Collaboration), *Eur. Phys. J. A* **49**, 156 (2013).
- [13] S. Marrone *et al.* (n\_TOF Collaboration), *Nucl. Instrum. Methods A* **517**, 389 (2004).
- [14] S. Andriamonje, M. Calviani, Y. Kadi, R. Losito, V. Vlachoudis, E. Berthoumieux, F. Gunsing, A. Giganon, Y. Giomataris, C. Guerrero, R. Sarmento, P. Schillebeeckx, and P. Siegler (n\_TOF Collaboration), *J. Korean Phys. Soc.* **59**, 1597 (2011).
- [15] D. B. Gayther, *Metrologia* **27**, 221 (1990).
- [16] International Evaluation of Neutron Cross-Section Standards, Technical Report Series (International Atomic Energy Agency, Vienna, 2007).
- [17] F. Belloni, S. Andriamonje, E. Berthoumieux, M. Brugger, M. Calviani, E. Chiaveri, N. Colonna, Y. Giomataris, C. Guerrero, F. Gunsing, Y. Kadi, F. J. Iguaz, M. Kebbiri, E. Lebbos, R. Losito, J. Pancin, T. Papaevangelou, V. Vlachoudis, and C. Weiss (n\_TOF Collaboration), *Phys. Scr.* **2012**, 014004 (2012).
- [18] J. Pancin *et al.* (n\_TOF Collaboration), *Nucl. Instrum. Methods A* **524**, 102 (2004).
- [19] N. M. Larson, Updated User's Guide for SAMMY: Multilevel R-matrix Fits to Neutron Data Using Bayes Equations, ORNL/TM-9179/R8, ORNL, Oak Ridge, Tennessee, USA (2008).
- [20] C. Guerrero *et al.* (n\_TOF Collaboration), *Nucl. Instrum. Methods A* **608**, 424 (2009).
- [21] U. Abbondanno *et al.* (n\_TOF Collaboration), *Nucl. Instrum. Methods A* **538**, 692 (2005).
- [22] E. Berthoumieux, Preliminary Report on BaF<sub>2</sub> Total Absorption Calorimeter Test Measurement, Technical Report (CEASaclay/DAPNIA/SPhN, 2004).
- [23] S. Marrone *et al.*, *Nucl. Instrum. Methods A* **568**, 904 (2006).
- [24] S. Kopecky, P. Siegler, and A. Moens, in *Proceedings of the International Conference on Nuclear Data for Science and Technology-ND 2007* (EDP Sciences, Nice, France, 2007), pp. 623–626.
- [25] P. Schillebeeckx, A. Borella, J. Drohe, R. Eykens, S. Kopecky, C. Massimi, L. Mihailescu, A. Moens, M. Moxon, and R. Wynants, *Nucl. Instrum. Methods A* **613**, 378 (2010).
- [26] P. Schillebeeckx, B. Becker, Y. Danon, K. Guber, H. Harada, J. Heyse, A. Junghans, S. Kopecky, C. Massimi, M. Moxon, N. Otuka, I. Sirakov, and K. Volev, *Nucl. Data Sheets* **113**, 3054 (2012), special issue on nuclear reaction data.
- [27] C. Nästren, M. Holzhäuser, A. Fernandez, C. Brossard, F. Wastin, H. Ottmar, and J. Somers, Fabrication of Am samples for neutron cross-section measurements at JRC-IRMM Geel, Technical Report No. JRC-ITU-TN-2006/34 (JRC-ITU, 2011).
- [28] C. Sage, V. Semkova, O. Bouland, P. Dessagne, A. Fernandez, F. Gunsing, C. Nästren, G. Noguère, H. Ottmar, A. J. M. Plompen, P. Romain, G. Rudolf, J. Somers, and F. Wastin, *Phys. Rev. C* **81**, 064604 (2010).
- [29] H. Tagziria, J. Bagi, B. Pedersen, and P. Schillebeeckx, *Nucl. Instrum. Methods A* **691**, 90 (2012).
- [30] T. Wright *et al.* (n\_TOF Collaboration), *Phys. Rev. C* **96**, 064601 (2017).
- [31] E. Mendoza *et al.* (n\_TOF Collaboration), *Phys. Rev. C* **90**, 034608 (2014).
- [32] C. Guerrero *et al.* (n\_TOF Collaboration), *Phys. Rev. C* **85**, 044616 (2012).
- [33] A. Krása and A. Plompen, Gamma-rays from a <sup>241</sup>AmO<sub>2</sub> source in an Al<sub>2</sub>O<sub>3</sub> matrix, Technical Report No. EUR 24818 EN (JRC-IRMM, 2011).
- [34] J. Balibrea-Correa *et al.* (n\_TOF Collaboration), *EPJ Web Conf.* **146**, 11021 (2017).
- [35] J. Tain and D. Cano-Ott, *Nucl. Instrum. Methods A* **571**, 719 (2007).
- [36] S. Agostinelli *et al.* (GEANT4 Collaboration), *Nucl. Instrum. Methods A* **506**, 250 (2003).
- [37] J. Allison *et al.*, *Nucl. Instrum. Methods A* **835**, 186 (2016).
- [38] C. Guerrero, D. Cano-Ott, E. Mendoza, J. Taín, A. Algora, E. Berthoumieux, N. Colonna, C. Domingo-Pardo, E. González-Romero, M. Heil, D. Jordán, F. Käppeler, C. Lampoudis, T. Martínez, C. Massimi, and R. Plag, *Nucl. Instrum. Methods A* **671**, 108 (2012).
- [39] E. Mendoza *et al.* (n\_TOF Collaboration), The Am-243 neutron capture measurement at the n\_TOF facility, in *Capture Gamma-Ray Spectroscopy and Related Topics* (World Scientific, Singapore, 2013), Chap. 60, pp. 442–449, [http://www.worldscientific.com/doi/pdf/10.1142/9789814383646\\_0060](http://www.worldscientific.com/doi/pdf/10.1142/9789814383646_0060).
- [40] E. Mendoza, Measurement of the Am243 capture cross section at the n\_TOF facility, Ph.D. thesis, Universidad Complutense de Madrid (2014).
- [41] E. Mendoza, D. Cano-Ott, C. Guerrero, and E. Berthoumieux, *Nucl. Instrum. Methods A* **768**, 55 (2014).
- [42] E. Mendoza *et al.* (n\_TOF Collaboration), High background induced pulse pile-up corrections for digitized signals from a BaF<sub>2</sub> calorimeter, *Nucl. Instrum. Methods A* (to be published).
- [43] R. L. Macklin, J. Halperin, and R. R. Winters, *Nucl. Instrum. Methods* **164**, 213 (1979).

- [44] The JEFF team, JEFF-3.2: Evaluated nuclear data library, OECD/NEA Data Bank (2014), <http://www.oecd-nea.org/dbdata/jeff>.
- [45] S. Oh and L. C. Leal, SUGGEL: A program suggesting the orbital angular momentum of a neutron resonance from the magnitude of its neutron width, Technical Report No. ORNL/TM-2000/314 (ORNL, Oak Ridge, Tennessee, USA, 2001).
- [46] J. Goorley *et al.*, Initial MCNP6 Release Overview - MCNP6 version 1.0, Technical Report No. LA-UR-13-22934 (LANL, Los Alamos, New Mexico, USA, 2013).
- [47] R. Capote *et al.*, *Nucl. Data Sheets* **110**, 3107 (2009).
- [48] J. Lerendegui-Marco *et al.* (n\_TOF Collaboration), *Phys. Rev. C* **97**, 024605 (2018).
- [49] F. H. Fröhner, *Nucl. Sci. Eng.* **103**, 119 (1989).
- [50] W. Hauser and H. Feshbach, *Phys. Rev.* **87**, 366 (1952).
- [51] H. Harada, M. Ohta, A. Kimura, K. Furutaka, K. Hirose, K. Hara, T. Kin, F. Kitatani, M. Koizumi, S. Nakamura, M. Oshima, Y. Toh, M. Igashira, T. Katabuchi, M. Mizumoto, K. Kino, Y. Kiyonagi, T. Fujii, S. Fukutani, J. Hori, and K. Takamiya, *Nucl. Data Sheets* **119**, 61 (2014).
- [52] M. Jandel, T. A. Bredeweg, E. M. Bond, M. B. Chadwick, R. R. Clement, A. Couture, J. M. O'Donnell, R. C. Haight, T. Kawano, R. Reifarth, R. S. Rundberg, J. L. Ullmann, D. J. Vieira, J. B. Wilhelmy, J. M. Wouters, U. Agvaanluvsan, W. E. Parker, C. Y. Wu, and J. A. Becker, *Phys. Rev. C* **78**, 034609 (2008).
- [53] G. Vanpraet, E. Cornelis, S. Raman, and G. Rohr, *Radiat. Eff.* **93**, 157 (1986).
- [54] D. Gayther and B. Thomas, in *Proceedings of the 4th All-Union Conf. on Neutron Phys.* (Kiev, 1977), Vol. 3, p. 3.
- [55] L. W. Weston and J. H. Todd, *Nucl. Sci. Eng.* **61**, 356 (1976).
- [56] S. M. Kalebin, V. S. Artamonov, R. N. Ivanov, G. V. Pukolaine, T. S. Belanova, A. G. Kolesov, and V. A. Safonov, *At. Energ.* **40**, 303 (1976).
- [57] H. Derrien and B. Lucas, in *Proceedings of the International Conference on Nuclear Cross-Section and Technology* (National Bureau of standards, Washington DC, 1975), Vol. 2, p. 637, <https://nvlpubs.nist.gov/nistpubs/Legacy/SP/nbsspecialpublication425v2.pdf>.
- [58] G. G. Slaughter, J. A. Harvey, and R. C. Block, High resolution total cross section measurements on Np237 and Am241, ORNL-3085 (ORNL, Oak Ridge, Tennessee, USA, 1961), p. 42.
- [59] J. V. Adamchuk, V. F. Gerasimov, B. V. Efimov, V. S. Zenkevich, V. I. Mostovoy, M. I. Pevzner, A. P. Tsitovich, A. A. Chernyshov, and S. S. Moskalev, in *Proceedings of the International Conference on the Peaceful Uses of Atomic Energy*, Geneva (United Nations publication, New York, 1955), Vol. 4, p. 259.
- [60] G. Noguere, O. Bouland, S. Kopecky, C. Lampoudis, P. Schillebeeckx, A. Plompen, F. Gunsing, C. Sage, and I. Sirakov, *Phys. Rev. C* **92**, 014607 (2015).
- [61] M. Chadwick *et al.*, *Nucl. Data Sheets* **112**, 2887 (2011), special issue on ENDF/B-VII.1 Library.
- [62] K. Shibata, O. Iwamoto, T. Nakagawa, N. Iwamoto, A. Ichihara, S. Kunieda, S. Chiba, K. Furutaka, N. Otuka, T. Ohsawa, T. Murata, H. Matsunobu, A. Zukeran, S. Kamada, and J. Katakura, *J. Nucl. Sci. Technol.* **48**, 1 (2011).
- [63] N. Shinohara, Y. Hatsukawa, K. Hata, and N. Kohno, *J. Nucl. Sci. Technol.* **34**, 613 (1997).
- [64] V. D. Gavrilov, V. A. Goncharov, V. V. Ivanenko, V. N. Kustov, and V. P. Smirnov, *At. Energ.* **41**, 185 (1976).
- [65] R. M. Harbour, K. W. MacMurdo, and F. J. McCrosson, *Nucl. Sci. Eng.* **50**, 364 (1973).
- [66] E. Hellstrand, J. Phelps, and C. Sastre, Brookhaven Natl. Lab. BNL **50242**, 577 (1970).
- [67] M. A. Bak, A. S. Krivokhatskii, K. A. Petrzhak, Y. G. Petrov, Y. F. Romanov, and E. A. Shlyamin, *At. Energ.* **23**, 1059 (1967).
- [68] S. Nakamura, M. Ohta, H. Harada, T. Fujii, and H. Yamana, *J. Nucl. Sci. Technol.* **44**, 1500 (2007).
- [69] N. L. Maidana, M. S. Dias, and M. F. Koskinas, *Radiochim. Acta* **86**, 419 (2001).
- [70] R. A. Deal and R. P. Schuman, Washington AEC Office Rep. **1053**, 76 (1964).
- [71] H. Harada *et al.*, file EXFOR 23172.002, retrieved from the IAEA Nuclear Data Services website, <http://www-nds.iaea.org/EXFOR/23172.002>.
- [72] B. Geslot, A. Gruel, P. Ros, P. Blaise, P. Leconte, G. Noguere, L. Mathieu, D. Villamarin, V. Becares, A. Plompen, S. Kopecky, and P. Schillebeeckx, *EPJ Web Conf.* **146**, 06016 (2017).
- [73] G. Žerovnik, P. Schillebeeckx, B. Becker, L. Fiorito, H. Harada, S. Kopecky, V. Radulović, and T. Sano, *Nucl. Instrum. Methods A* **877**, 300 (2018).